Materials Science and Engineering B 324 (2026) 118997

Contents lists available at ScienceDirect

Materials Science & Engineering B

journal homepage: www.elsevier.com/locate/mseb

Oxygen sensing properties of room temperature phosphorescent halogenated hexahydroxanthene derivatives

Mageshwari Anandan [a], Sohrab Nasiri [b,c], Praveen B. Managutti [d], Sharmarke Mohamed [d], Jean Michel Nunzi [e], Venkatramaiah Nutalapati [a,f,*], Yuning Li [c,*]

[a] Functional Materials Laboratory, Department of Chemistry, Faculty of Engineering and Technology, SRM Institute of Science and Technology, Kattankulathur, Tamil Nadu 603203, India
[b] Faculty of Mechanical Engineering and Design, Kaunas University of Technology, Studentu Street 56, Kaunas, LT 51373, Lithuania
[c] Department of Chemical Engineering and Waterloo Institute for Nanotechnology (WIN), University of Waterloo, 200 University Ave West, Waterloo, Ontario N2L 3G1, Canada
[d] Chemical Crystallography Laboratory, Khalifa University of Science and Technology, Abu Dhabi PO Box 127788, United Arab Emirates
[e] Department of Physics, Engineering Physics & Astronomy, Queens University, Kingston K7L-3N6, Ontario, Canada
[f] Centre for Interdisciplinary Research (CIDR), SRM University-AP, Amaravati, Andhra Pradesh 522 240, India

ARTICLE INFO

Keywords:
Hexahydroxanthene
Halogens
Phosphorescence
Room temperature phosphorescence
Oxygen sensing

ABSTRACT

A series of halogenated hexahydroxanthene (XAN) derivatives, XAN-F, XAN-Cl, XAN-Br, XAN-I, and XAN-5F, were synthesized to investigate their room-temperature phosphorescence (RTP) and optical oxygen-sensing performance. Single-crystal X-ray diffraction revealed that heavier halogens (Br and I) induce nearly orthogonal dihedral angles between the xanthene and phenyl rings (84.87° for XAN-Br and 86.18° for XAN-I), enhancing molecular rigidity and spin–orbit coupling (SOC). This structural configuration promotes efficient intersystem crossing (ISC) and suppresses nonradiative decay, enabling pronounced RTP. In contrast, XAN-Ph without halogen substitution displayed fluorescence, while derivatives bearing lighter halogens (F, Cl, and 5F) exhibited only low-temperature phosphorescence. Thin films of XAN-Br and XAN-I containing 1 wt% Zeonex displayed strong RTP with lifetimes up to 4.48 ms. They also showed exceptional ISC quantum yields (93.02 % for XAN-Br and 93.51 % for XAN-I) and large vacuum-to-air photoluminescence intensity ratios (14.67 and 15.33, respectively). These features translated to excellent oxygen sensitivity, with Stern-Volmer quenching constants (K_{sv}) of 6.08×10^{-5} and 1.11×10^{-4} ppm^{-1} for XAN-Br and XAN-I, respectively. This high oxygen sensitivity arises from efficient triplet–triplet energy transfer from the XAN's triplet excited state to ground-state triplet oxygen, leading to nonradiative quenching. With their metal-free composition, efficient RTP, excellent oxygen responsiveness, and good solution-processability into thin films, XAN-Br and XAN-I represent promising candidates for use in optical oxygen sensors for biomedical diagnostics, food preservation, and environmental monitoring.

* Corresponding authors.

1. Introduction

Oxygen sensors are essential across a broad range of fields, including biomedicine, environmental monitoring, industrial process control, combustion systems, and safety diagnostics, where accurate oxygen detection contributes to enhanced efficiency, safety, and sustainability [1]. In biomedical applications, for example, sensors with sensitivity in the range of 0.5–3.0 % O_2 are well suited for imaging tumor hypoxia [2], while those with sensitivity in the 5–15 % range are effective for monitoring blood oxygenation [3]. Among various sensing platforms, room-temperature phosphorescence (RTP)-based optical oxygen sensors have gained increasing attention as an alternative to conventional electrochemical sensors (e.g., Clark electrodes), owing to their distinct advantages: non-(or negligible) consumptive oxygen detection, high precision, long-term operational stability, miniaturization potential, and real-time visual feedback through emission color changes [4,5]. RTP materials feature long emission lifetimes, large Stokes shifts, and high signal-to-noise ratios, with luminescence often visible to the naked eye

* Corresponding author.
E-mail addresses: venkatramaiah.n@srmap.edu.in, nvenkat83@gmail.com (V. Nutalapati), yuning.li@uwaterloo.ca (Y. Li).

https://doi.org/10.1016/j.mseb.2025.118997
Received 23 May 2025; Received in revised form 8 September 2025; Accepted 4 November 2025
Available online 10 November 2025
0921-5107/© 2025 The Author(s). Published by Elsevier B.V. This is an open access article under the CC BY license (http://creativecommons.org/licenses/by/4.0/).

[6]. RTP occurs from spin-forbidden radiative transitions from the triplet excited state $^3T_1$ to the singlet ground state $^1S_0$, leading to long-lived luminescence with lifetimes ranging from microseconds to seconds or even longer at room temperature [7]. Achieving robust RTP under ambient conditions requires (i) efficient triplet population via intersystem crossing (ISC), typically by enhancing spin–orbit coupling (SOC), and (ii) suppression of nonradiative deactivation of triplet excitons [8]. Molecular oxygen, a powerful triplet quencher, has long been regarded as a primary obstacle to RTP, motivating approaches that limit O_2 exposure, such as crystallization [9], encapsulation/barrier layers [10], and polymer-matrix embedding [11]. The oxygen sensitivity of RTP materials stems from the fact that molecular oxygen, which exists in a triplet ground state ($^3\Sigma_g^-$), efficiently quenches the excited triplet states of phosphorescent molecules via energy transfer, resulting in non-radiative deactivation [7,8]. While this oxygen-induced quenching is often considered detrimental in other applications, it forms the basis of RTP-based oxygen sensing, where suppressed phosphorescence intensity or lifetime is directly correlated to oxygen concentration [12–14]. Organic RTP materials are particularly appealing due to their low cost, synthetic tunability, environmental friendliness, and compatibility with flexible substrates. They have been explored for applications such as chemical and biological sensing, time-gated bioimaging, anti-counterfeiting, optical data storage, quantum computing, photodynamic therapy, and smart packaging technologies [6,9]. However, unlike organometallic RTP systems that leverage heavy transition metals (e.g., Pd, Pt, Ru) to enhance ISC, purely organic RTP materials suitable for oxygen sensing remain limited [15]. This is largely due to their inherently low ISC efficiency, high nonradiative decay rates, and restricted oxygen diffusion.

Among recent developments, some organoboron compounds have shown promising RTP and oxygen-sensing performance. For example, Zang et al. reported an organoboron-based iodinated polymeric dye (BF_2dbm(*I*)PLA) showing weak fluorescence and strong RTP, which exhibited a high oxygen quenching constant ($K_{sv} = 0.06 \times 10^{-4}$ ppm^{-1}), attributed to the iodine-induced heavy-atom effect [16]. Zhou et al. introduced TBBU, a triphenylamine boronate ester with a donor–π–acceptor structure, achieving efficient RTP and visual oxygen detection facilitated by its porous crystal packing [17]. However, subsequent work by Wu et al. revealed that the observed RTP in TBBU was due to trace impurities of DTBU, and the RTP behavior was attributed to a Dexter energy transfer process between host (TBBU) and dopant species (DTBU) [18]. Hamzehpoor et al. synthesized organoboron-based RTP covalent organic frameworks (COFs) through condensation of *p*-phenylene diboronic acids (PBA) in the presence of a small amount of dibrominated (BrPBA) derivative [19]. The resulting COF, with 13 % BrPBA, exhibited efficient RTP and good oxygen sensing capability in a wide concentration range from 762 Torr to 10^{-5} Torr of partial oxygen pressure, achieving up to ~70 % quenching efficiency. This performance was attributed to enhanced ISC facilitated by the Br atoms and the intrinsic porosity of the COF, which promotes oxygen diffusion.

Xanthene-based fluorophores including fluorescein, eosin, and rhodamine dyes have long been known for their photostability and ease of chemical modification [14,20,21]. While hexahydroxanthene itself is non-fluorescent, many of its derivatives exhibit rich emission behavior and demonstrate biological activity, enabling their use in sensors, drug development, and optical devices [22]. Additionally, hexahydroxanthenes exhibit notable biological activities, including antibacterial, anti-inflammatory, and anticancer properties, making them valuable in drug development. Consequently, hexahydroxanthenes have diverse applications in pharmaceuticals, materials science, and optical technologies. The classical method to extend emission wavelengths and achieve fluorescence is to increase the π-conjugation of the original xanthene dyes, the so-called π-extension strategy [17,18]. Although xanthene dyes can exhibit stable RTP, their sensitivity toward oxygen sensing is generally limited. To address this, Wang et al. developed selenoxanthene-based donor–acceptor RTP emitters through substitution of the central oxygen with selenium and the incorporation of electron-withdrawing ketones. These molecules achieved high sensitivity for oxygen detection, with the 3-substituted isomer offering an impressive oxygen detection capability [19,20].

In this study, we report six halogenated derivatives based on a hexahydro-1H-xanthene-derived fluorone core bearing two carbonyl (C=O) groups in a tricyclic scaffold (Scheme 1). By systematically introducing halogen substituents (F, Cl, Br, I, and 5F) on the peripheral phenyl ring, we investigate how halogen identity and placement influence their structural, photophysical, electrochemical, and oxygen-sensing properties. The incorporation of heavier halogens, specifically Br and I, is expected to enhance ISC via the heavy atom effect, facilitating ambient RTP and improving oxygen sensitivity. These new xanthene-based derivatives exhibit enhanced oxygen sensitivity. Their facile synthesis, polymer compatibility, and efficient ambient RTP response make them promising candidates for integration into biomedical sensors, food packaging, wearable oxygen monitors, and environmentally responsive devices.

2. Experimental

2.1. Synthesis of 9-(4-halophenyl)-3,3,6,6-tetramethyl-3,4,5,6,7,9-hexahydro-1H-xanthene-1,8(2H)-dione

General procedure: A mixture of aldehyde (1 eq) and dimedone (2 eq) was dissolved in 10 mL of DMF in a 50 mL round-bottom flask, followed by the addition of a catalytic amount of conc. HCl (5 mol%) under stirring. The reaction mixture was heated to reflux and maintained for 12 h, during which it gradually turned dark red. The progress of the reaction was monitored by TLC, which confirmed that no starting material was present. After the completion of the reaction, the mixture was cooled to room temperature and poured into ice water a brown solid was obtained. The solid was thoroughly washed with water, filtered and dried for 5 days at room temperature. Further, column chromatography was used to purify the compound using hexane and ethyl acetate (7:3, *v/v*).

2.1.1. Synthesis of 3,3,6,6-tetramethyl-9-phenyl-3,4,5,6,7,9-hexahydro-1H-xanthene-1,8(2H)-dione (XAN-Ph)

White solid with a yield of 87 %. ^{1}H NMR ($CDCl_3$, 300 MHz) (ppm): δ 7.28 (d, $J = 9$ Hz, 2H), 7.21 (t, $J = 6$ Hz, 2H), 7.09 (t, $J = 9$ Hz, 1H), 4.75 (s, 1H), 2.47 (s, 1H), 2.19 (q, $J = 15$ Hz, 4H), 1.10 (s, 1H) and 0.99 (s, 1H) ppm. ^{13}C{^{1}H} NMR ($CDCl_3$, 75 MHz): δ 196.42, 162.29, 144.10, 128.39, 128.05, 126.37, 115.67, 50.75, 40.88, 32.20, 31.84, 29.28 and 27.33 ppm. HR-MS (*m/z*) $[C_{52}H_{55}NO_6]^+$: Calcd. 350.4507 found 351.1963 $[M + H]^+$.

2.1.2. Synthesis of 9-(4-fluorophenyl)-3,3,6,6-tetramethyl-3,4,5,6,7,9-hexahydro-1H-xanthene-1,8(2H)-dione (XAN-F)

Beige-white solid with 82 % yield. ^{1}H NMR (500 MHz, $CDCl_3$) (ppm): δ 7.25–7.23(m, 2H), 6.92–6.87 (m, 2H), 4.73 (s, 1H), 2.46 (t, $J = 20$ Hz, 4H), 2.2(q, $J = 15$ Hz, 4H), 1.10(s, 6H) and 0.99(s, 6H). ^{13}C{^{1}H} NMR ($CDCl_3$, 75 MHz): δ 196.48, 162.99, 162.37, 159.76, 139.94, 129.90, 129.79, 115.5, 114.99, 114.71, 50.71, 40.84, 32.22, 31.21, 29.28, and 27.29 ppm. HR-MS (*m/z*) $[C_{23}H_{25}NO_5]^+$: Calcd. 368.4412 found 369.1845 $[M + H]^+$.

2.1.3. Synthesis of 9-(4-chlorophenyl)-3,3,6,6-tetramethyl-3,4,5,6,7,9-hexahydro-1H-xanthene-1,8(2H)-dione (XAN-Cl)

Beige-white solid with 80 % yield. ^{1}H NMR (300 MHz, $CDCl_3$) (ppm): δ 7.2(q, $J = 10$ Hz, 2H), 4.71 (s, 1H), 2.46 (t, $J = 20$ Hz, 4H), 2.2 (q, $J = 15$ Hz, 4H), 1.10(s, 6H) and 0.99(s, 6H). ^{13}C{^{1}H} NMR ($CDCl_3$, 75 MHz): δ 196.39, 162.46, 142.72, 132.03, 129.79, 128.23, 115.26, 50.76, 40.84, 32.22, 31.47, 29.29 and 27.29 ppm. HR-MS (*m/z*) $[C_{23}H_{25}NO_5]^+$: Calcd. 384.8958 found 385.1546 $[M + H]^+$.

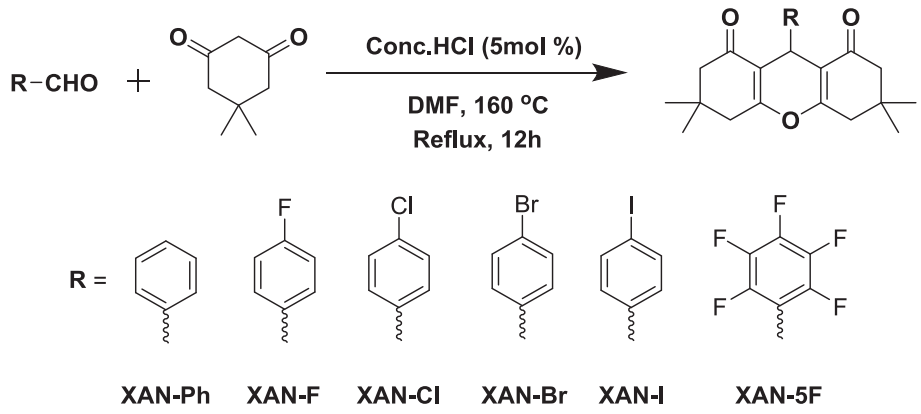

Scheme 1. Synthetic route of halophenylhexahydroxanthene derivatives.

2.1.4. Synthesis of 9-(4-bromophenyl)-3,3,6,6-tetramethyl-3,4,5,6,7,9-hexahydro-1H-xanthene-1,8(2H)-dione (XAN-Br)

White solid with a yield of 85 %. ^{1}H NMR ($CDCl_3$, 300 MHz) (ppm): δ 7.33(d, $J = 15$ Hz, 2H), 7.17 (d, $J = 9$ Hz, 2H), 4.69(s, 1H), 2.53–2.40(m, 4H), 2.27–2.13 (m, 4H), 1.10(s, 6H) and 0.99 (s, 6H). ^{13}C{^{1}H} NMR ($CDCl_3$, 75 MHz): δ 196.38, 162.49, 143.24, 131.01, 130.19, 120.24, 115.18, 50.69, 40.84, 32.21, 31.56, 29.28 and 27.30 ppm. HR-MS (*m/z*) $[C_{23}H_{25}NO_5]^{+}$: Calcd. 429.3468 found 430.1082 $[M + H]^{+}$.

2.1.5. Synthesis of 9-(4-iodophenyl)-3,3,6,6-tetramethyl-3,4,5,6,7,9-hexahydro-1H-xanthene-1,8(2H)-dione (XAN-I)

Beige-white solid with 79 % yield. ^{1}H NMR (500 MHz, $CDCl_3$) (ppm): δ 7.24(d, $J = 10$ Hz, 2H), 7.04 (d, $J = 5$ Hz, 2H), 4.68 (s, 1H), 2.45(t, $J =$ 15 Hz, 4H), 2.2 (q, $J = 15$ Hz, 4H), 1.10(s, 6H) and 0.99(s, 6H) ^{13}C{^{1}H} NMR ($CDCl_3$, 75 MHz): δ 196.39, 162.48, 143.94, 137.12, 130.52, 115.15, 91.98, 50.69, 40.84, 32.22, 31.69, 29.29 and 27.33 ppm. HR-MS (*m/z*) $[C_{23}H_{25}NO_5]^{+}$: Calcd. 476.0848 found 477.0892 $[M + H]^{+}$.

2.1.6. Synthesis of 3,3,6,6-tetramethyl-9-(perfluorophenyl)-3,4,5,6,7,9-hexahydro-1H-xanthene-1,8(2H)-dione (XAN-5F)

Brown solid with a yield of 55 %. ^{1}H NMR ($CDCl_3$, 300 MHz) (ppm): δ 4.83–4.67(m, 1H), 3.3 (s, 1H) 2.81 (s, 1H) 2.41 (S, 2H), 2.28 (s, 1H), 1.06 (s, 12H). ^{13}C{^{1}H} NMR ($CDCl_3$, 75 MHz): δ 198.33, 164.34, 108, 107.96, 106.09, 106.06, 50.49, 41.03, 32.16, 31.59 and 28.32 ppm. The final product (XAN 5F) was obtained as a HR-MS (*m/z*) $[C_{23}H_{21}F_5O_3]^{+}$: Calcd. 440.4031 found 441.1499 $[M + H]^{+}$.

3. Results and discussion

3.1. Molecular design and synthesis

Different synthetic methodologies with specialized catalysts such as Fe-zeolite or Cu(II) complexes were used to develop hexyhydroxanthene derivatives. Compared to the previously reported methods (Table S5), the current approach using 5 mol% HCl in DMF at 160 °C for 12 h offers several advantages in terms of simplicity, accessibility, and cost-effectiveness. This straightforward setup eliminates the need for specialized equipment like ultrasound systems or electrolysis setups, making it easier to implement in standard laboratory conditions. Additionally, the use of HCl ensures consistent catalytic performance without concerns related to catalyst deactivation or handling issues often associated with multi-component or metal-based systems. Acid-catalyzed one-pot condensation reaction was carried out between dimedone, and the respective aldehyde to obtain XAN-Ph, XAN-F, XAN-Cl, XAN-Br, XAN-I and XAN-5F in good yields (55–87 %) (Scheme 1). The ^{1}H and ^{13}C NMR and HRMS spectra are provided in Figs. S8-S25. For all the derivatives, two singlets observed between δ 0.9 to 1.2 ppm in their ^{1}H NMR spectra correspond to the four methyl groups attached to the hexahydroxanthene tricyclic core, a tertiary proton appeared as a singlet between δ 4.6–4.9 ppm and the aromatic protons appeared between δ 7.1 to 7.5 ppm. The HRMS spectra show the characteristic $[M + H]^{+}$ molecular ion peaks, confirming the identity of the desired products.

3.2. Time-dependent density functional theory (TD-DFT) studies

To reveal the relationship between orbital distributions and optimized geometries, the highest occupied molecular orbital (HOMO) and the lowest unoccupied molecular orbital (LUMO) (Fig. 1) were calculated using DFT (Gaussian 09 W- DFT/6–311 + G (d, p)) [23]. In Fig. 1, the LUMO is located on the xanthene core, indicating its role as the electron-accepting unit. Among the compounds, XAN-Ph exhibits the highest LUMO energy (−1.98 eV), which decreases with halogen substitution, reaching −2.41 eV for XAN-5F. In addition, the HOMO energy levels representative of the donor units are −6.51, −6.61, −6.65, −6.52, −6.26 and − 7.04 eV for XAN-Ph, XAN-F, XAN-Cl, XAN-Br, XAN-I and XAN-5F, respectively (Table 1). In all cases except XAN-5F, the HOMO is distributed mainly over the phenyl ring. In XAN-5F, both HOMO and LUMO are delocalized across the xanthene core. This behavior is attributed to the strong electron-withdrawing inductive effects of the five fluorine atoms, which reduces charge transfer (CT) character and increases the delocalization of orbitals [24]. In XAN-5F, the inductive electron-withdrawing effect of the fluorine atoms reduces the internal electron push-pull (CT character) so that the π electrons can be distributed more evenly over the xanthene core. The fluorine atoms lower the electron density evenly and reduce the donor-acceptor polarity. This suppresses the CT character and both HOMO and LUMO are distributed more evenly across the molecule (delocalized) [23,24]. Besides the significant charge transfer behavior, which indicates a spatial separation of the charge distributions in XAN-Ph, F, Cl, Br, I, and 5F, this can lead to a weak exchange interaction between the electrons involved, resulting in minimal energy splitting between singlet (S_1) and triplet (T_1) states [25]. It is important to emphasize that the presence of halogens on the phenyl ring leads to a significant reduction in HOMO and LUMO values, especially in the presence of pentafluorobenzene. This is because the halogens also exhibit a resonance effect that can either donate or withdraw electron density easily when the withdrawal makes the molecular orbitals more stable and shifts their energy levels downward [26]. Among all the derivatives, the non-halogenated XAN-Ph showed the largest difference between the HOMO and LUMO energy levels (E_g), which can be attributed to the phenyl group that neither withdraws nor donates electron density compared to the halogen-substituted derivatives [27]. Moreover, among the halogenated derivatives, XAN-I exhibits the lowest E_g (4.16 eV), indicating stronger stabilization of the LUMO, while XAN-5F shows the highest E_g (4.63 eV), indicating strong electron-withdrawing effects that lower the HOMO more than the LUMO, and XAN-Br has a slightly lower E_g than XAN-Cl, implying that

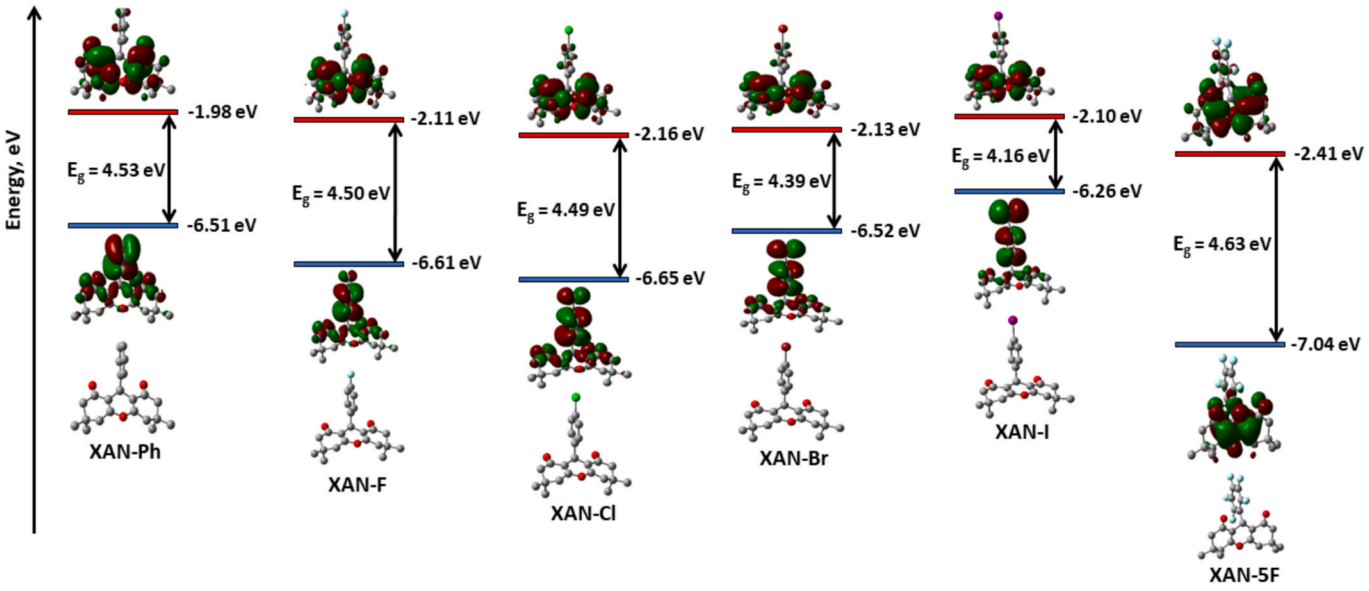

Fig. 1. DFT calculated HOMO-LUMO energy, energy gap profiles and special distributions.

Table 1
The extracted values from DFT and electrochemical properties.

Compound	a) $\lvert E^{IP}\rvert$, eV	b) E^{DFT}_{HOMO}, eV	c) E^{DFT}_{LUMO}, eV	d) E_g^{Opt} (film), eV	e) E^{HOMO}_{CV}, eV	f) EA_{CV}, eV	g) E^{film}_{S}, eV	h) E^{film}_{T}, eV
XAN-Ph	6.49	−6.51	−1.98	3.33	−5.91	2.58	3.06	2.91
XAN-F	6.29	−6.61	−2.11	3.67	−5.87	2.20	3.32	3.01
XAN-Cl	6.40	−6.65	−2.16	3.38	−5.90	2.52	3.25	3.13
XAN-Br	6.50	−6.52	−2.13	3.70	−6.20	2.50	3.30	2.93
XAN-I	6.28	−6.26	−2.10	3.11	−6.16	3.05	3.27	3.05
XAN-5F	6.63	−7.04	−2.41	3.17	−5.92	2.75	3.20	2.74

a) Extracted values from the onset of IP plot.
b) HOMO from DFT.
c) LUMO from DFT.
d) Calculated by the formula ($E_g^{opt} = \frac{1240}{\lambda_{edge}}$) from the edges of absorption spectrum of spin-coated derivatives on the films.
e) Calculated HOMO from CV curve by the formula [-(E onset of oxidation +4.8)] [28].
f) EA^{CV} from CV curve of dissolved compounds in DCM by the formula -(E^{HOMO}_{CV}-E_g^{opt}) [29].
g) The calculated singlet energy from onset PL spectra of spin-coated compounds on the films at 77K.
h) The calculated singlet energy from onset PH spectra of spin-coated compounds on the films at 77K.

the E_g decreases with increasing atomic size of the halogen substituents (I < Br < Cl). In addition, the absorption (ABS) spectra calculated from DFT are presented in Fig. S1.

3.3. Single crystal and powder X-ray diffraction

High-quality single crystals of the XAN derivatives were obtained by dissolving the compounds in a dichloromethane (DCM): methanol (1:4, *v/v*) mixture and allowed for slow evaporation at ambient temperature. Among them, XAN-F and XAN-Cl exhibited similar interactions to the reported structures [30]. X-ray crystallographic data and refinement parameters are summarized in Table S1. Fig. 2 represents the ORTEP diagrams (50 % of the thermal ellipsoids) of XAN-Ph, XAN-Br, XAN-I and XAN-5F and their overlay structures. Single-crystal XRD (SXRD) analysis revealed that the molecular stability arises from a complex network of intra- and intermolecular interactions, influenced by torsional effects between the xanthene tricyclic ring and the halophenyl group. XAN-Ph, XAN-Br and XAN-5F exhibited a monoclinic crystal system with space group of $P2_1$. In the crystal lattice of XAN-Ph, multiple C···H contacts (2.883, 2.924, 2.953, and 2.821 Å) indicate significant C-H···π interactions, contributing to the stabilization of the crystal packing. The C···O interaction (3.185 Å) suggests moderate carbonyl-based stabilization, while the C···C contact (3.362 Å) reflects weak π-π stacking, providing limited structural reinforcement. The O···H contact involving the xanthene tricyclic ring (2.554 Å) indicates a relatively strong hydrogen bond, enhancing overall lattice stability. The dihedral angle of 81.35° between the xanthene tricyclic ring and the phenyl unit. The crystal structure of XAN-Br reveals that its crystalline stability is influenced by a combination of intermolecular interactions and molecular conformation. The O···C contacts (3.267 and 3.229 Å) suggest moderately strong carbonyl interactions, contributing to lattice stability. The C···C interactions (3.569 and 2.762 Å) suggest varying degrees of π-π stacking, with the shorter contact expected to enhance stability more effectively. The dihedral angle of 84.87° between the xanthene tricyclic ring and the bromophenyl unit indicates a slightly compressed conformation, which may influence molecular packing and electronic communication. For XAN-5F, its structural stability is realized through a combination of strong intermolecular and intramolecular interactions. Intermolecular interactions include F···H (2.448 and 2.482 Å), O···H (2.625, 2.556, and 2.684 Å), O···C (3.228 and 3.205 Å), C···C (3.318 Å), C···H (2.776 Å), C···F (3.080 and 3.047 Å), and H···H (2.120 Å), which collectively contribute to molecular packing and stability.

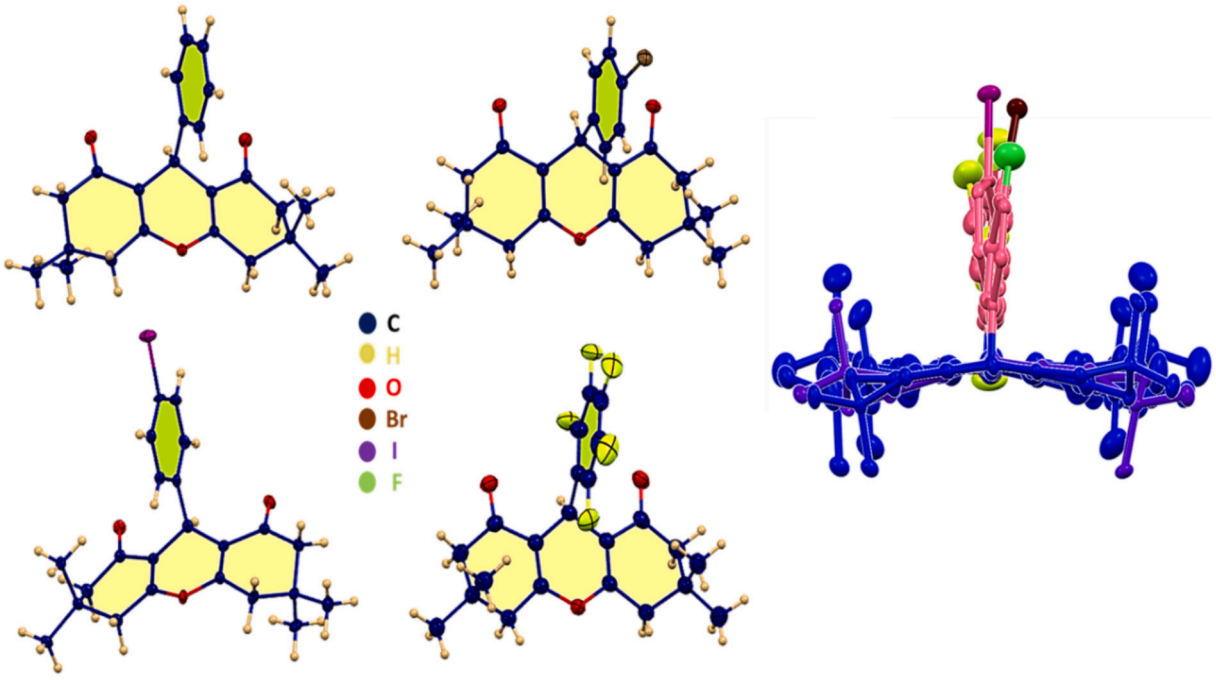

Fig. 2. Single crystal X-ray structures of different XAN derivatives with 50 % of the thermal ellipsoids.

Intramolecular interactions involving O···C (3.171, 3.195, 2.985, and 2.974 Å) and C···F (3.080 and 3.047 Å) further reinforce the internal structure. The dihedral angle of 88.39° between the xanthene tricyclic ring and the pentafluorophenyl ring suggests a nearly perpendicular orientation, minimizing steric hindrance and enhancing overall stability. These interactions, particularly those involving fluorine and oxygen, play a significant role in maintaining the robust crystalline framework of XAN-5F. XAN-I is arranged in an orthorhombic space group with a $P2_12_12_1$ spatial arrangement and its crystalline stability is influenced by a combination of intermolecular interactions and molecular geometry. The O···H interaction (2.452 Å) indicates a relatively strong hydrogen bond, playing a crucial role in reinforcing the lattice structure. Additionally, the H···H contacts (2.892 and 2.385 Å) are notably short, suggesting possible steric crowding or van der Waals interactions that may either stabilize or constrain molecular flexibility. The dihedral angle of 86.18° between the xanthene tricyclic ring and the iodophenyl unit further influences the packing arrangement. XAN- 5F demonstrates the strongest stability, featuring a diverse network of interactions such as F···H, O···H, C···C, and C···F contacts, with halogen bonding playing a key role in reinforcing the crystal structure. XAN-Br shows moderate stability, stabilized by O···C, Br···H, and Br···C interactions; however, the relatively longer Br-based contacts suggest weaker stabilization compared to XAN-5F. XAN-Ph appears to be the least stable, relying predominantly on weak C···H interactions and lacking significant strong directional bonding, making its structural stability more dependent on efficient packing. XAN-I exhibits a combination of moderate and weak interactions, featuring strong O···H bonding that enhances stability, though the presence of unusually short H···H contacts suggests potential steric strain. Overall, the strong interactions in XAN-I and XAN-Br minimize molecular vibrations, suppressing nonradiative decay and thus extending RTP lifetime. XAN-I (86.18°) and XAN-Br (84.87°) exhibit nearly perpendicular dihedral angles between the xanthene tricyclic ring and their respective halophenyl units. This rigid conformation restricts non-radiative relaxation, favoring efficient triplet emission. XAN-5F (88.39°) is even more rigid, but its RTP is weaker due to the lower SOC effect of fluorine. The packing and interaction modes of the crystal system are shown in the SI.

Powder XRD analysis was performed to investigate the phase characteristics and crystallite size of the derivatives, with the resulting spectra presented in **Fig. 3a**. The halogen substitution significantly affects the crystallinity and molecular packing. The sharp and intense peaks observed for XAN-Ph, XAN-Br, XAN-Cl and XAN-5F indicate their highly crystalline structures, while the broader and less intense peaks for XAN-I and especially for XAN-F indicate lower crystallinity or a more amorphous nature. Fluorine reduces XAN-F crystallinity by disrupting packing (steric bulk, weaker interactions) [31]. Based on the modified Scherrer method, Ln β (β is full width at half maximum of the peak in Radian) is calculated as Y-axis and Ln $\frac{1}{\text{Cos }(\theta)}$ (θ is the diffracted angle of the peak in Degree) as X-axis, and the linear fit is depicted in Fig. 3b. According to Eq. (1) [32], whose intercept can be obtained from linear fitting, K is the shape factor, which is usually assumed to be 0.89 for compounds, λ is the wavelength of radiation in nanometers (λ= 0.15405 nm for Cu Kα) and L is the crystallite size. The calculated crystallite sizes for XAN-Ph, F, Cl, Br, I and 5F are 58.10, 27.44, 58.10, 76.11, 81.63 and 3.86 nm, respectively. The notably smaller crystallite sizes for XAN-F and 5F indicate that the fluorine and the multiple fluorine atoms present a significant steric hindrance that disrupts the π-π stacking interactions and reduces crystallite growth [33].

$$e^{(\text{intercept})} = \frac{K\lambda}{L} \quad (1)$$

3.4. Study of FTIR and SEM

The Fourier transform infrared spectroscopy (FTIR) spectra of the XAN derivatives shown in Fig. 4a exhibit the characteristic vibrational bands corresponding to the functional groups of the XAN core structure [34]. Overall, the spectra are consistent across derivatives, with no major changes observed. However, a distinct band at ~855 cm^{-1} appears sharper in XAN-I compared to the other ones, which is attributed to the fact that iodine is the heaviest halogen, which has a lower frequency and stronger vibrational mode compared to F, Cl and Br. In addition, the C—I bond is weaker and more polarizable, resulting in a better defined absorption peak [35]. The C-X stretching vibrations (halogen-carbon) typically occur in the range of 500–800 cm^{-1}. Heavier halogens (I, Br, Cl) slightly shift the C═O stretching vibration to lower wavenumbers, indicating increased conjugation or interaction with the

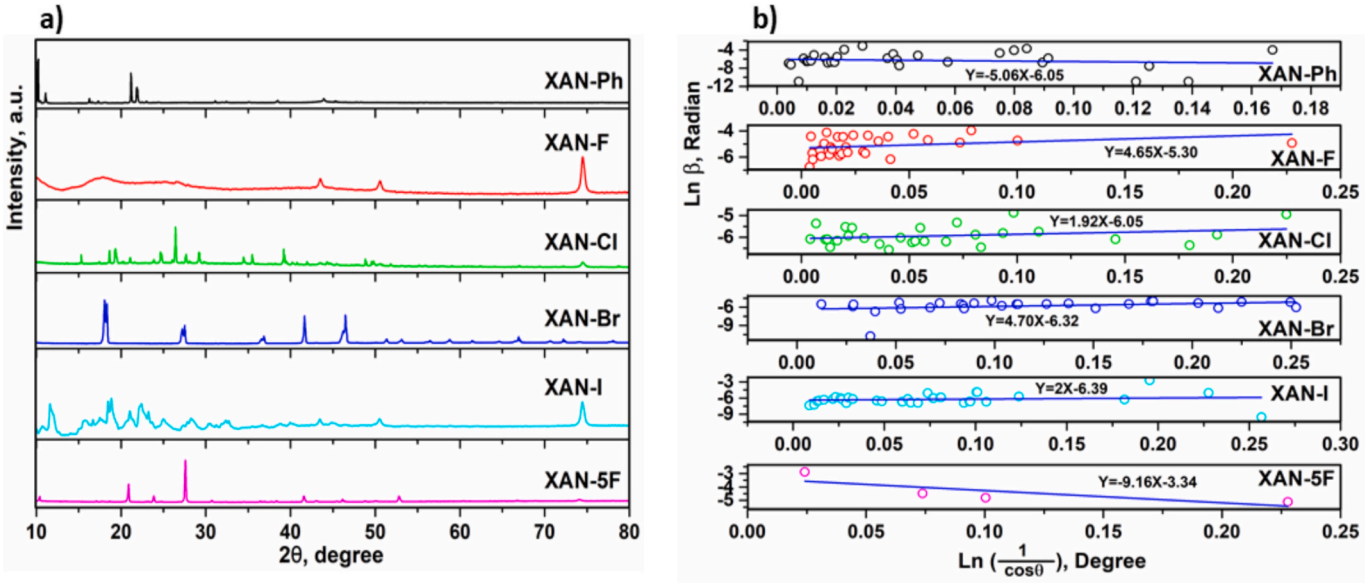

Fig. 3. a) powder X-ray diffraction and b) the linear plot of the Modified Scherrer Equation for the XAN derivatives.

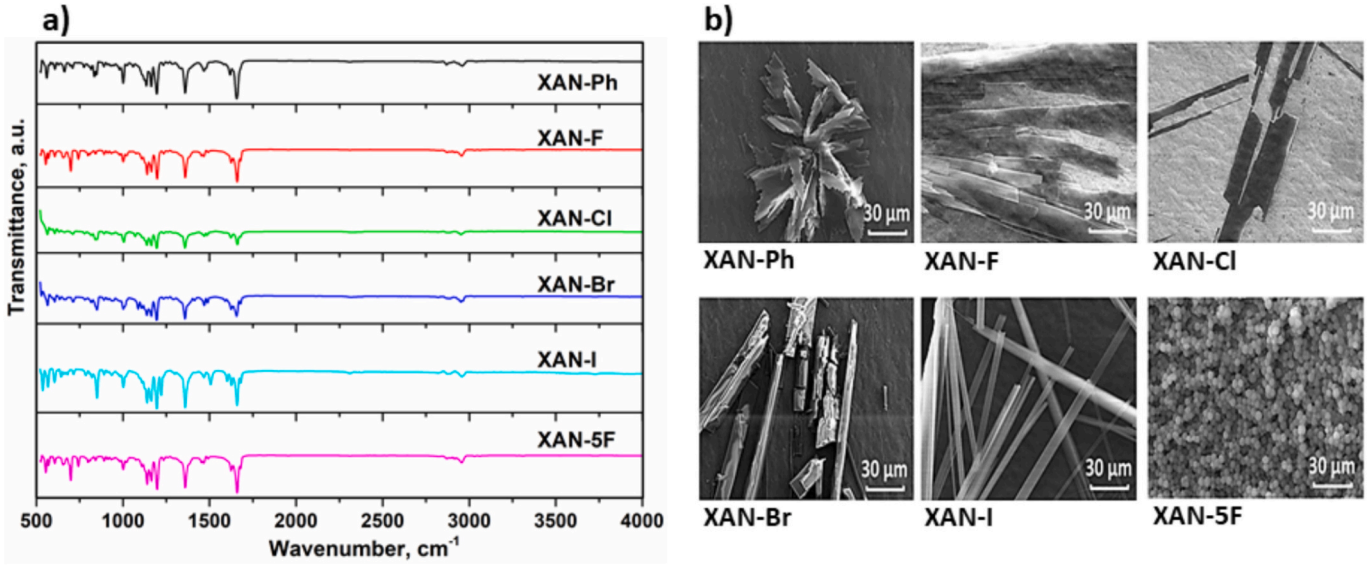

Fig. 4. a) FTIR spectrum and b) SEM images of the XAN derivatives.

molecular framework. In contrast, fluorinated derivatives (XAN-F and 5F) show C═O shifts due to strong inductive effects and steric hindrance [36]. A strong absorption band between ~1550–1750 cm^{-1} is observed for all derivatives, confirming the presence of carbonyl functional groups (C=O). The slight shifts of this peak between the different derivatives indicate variations in electron density and molecular interactions caused by halogen substitution [37]. Furthermore, the stretching bands from ~1000 to 1400 cm^{-1} correspond to the ether group (C-O-C), which is an essential feature of the XAN core structure. The region from 2700 to 3200 cm^{-1} contains absorption bands associated with both aromatic (sp^2) and aliphatic (sp^3) C—H bonds, confirming the presence of different structural components in the synthesized XAN derivatives [38]. Scanning electron microscopy (SEM) was used to examine the morphology of the XAN-Ph, —F, —Cl, —Br, —I and —5F (Fig. 4b). XAN-Ph and Br exhibit well-defined, leaf-shaped and elongated rod-shaped crystals, respectively, consistent with their high crystallinity observed in XRD patterns. In contrast, XAN-F and 5F show densely packed brick-like and granular structures, respectively. Morphological changes confirm that halogen substitution affects packing and crystallization.

3.5. *Ionization potential and electrochemical properties*

Ionization potential (IP) measurements and cyclic voltammetry (CV) analysis were conducted in the solid films and in DCM (10^{-3} M), respectively, to obtain the HOMO energy levels of the XAN derivatives. The resulting IP plot and CV curves are shown in Fig. 5a and b, respectively, with corresponding data summarized in Table 1. According to the IP measurements, the highest ionization energy (6.63 eV) was observed for XAN-5F, reflecting the strong electron-withdrawing nature of fluorine and enhanced oxidative stability. Conversely, XAN-I exhibited the lowest IP (6.28 eV), indicating that it is the easiest to ionize. This lower IP value can be attributed to high polarizability of iodine, which reduces orbital localization, raises the HOMO energy level, and consequently improves the hole injection properties [39]. The HOMO (E_{CV}^{HOMO}) and electron affinity (EA_{CV}) values of the compounds were derived from

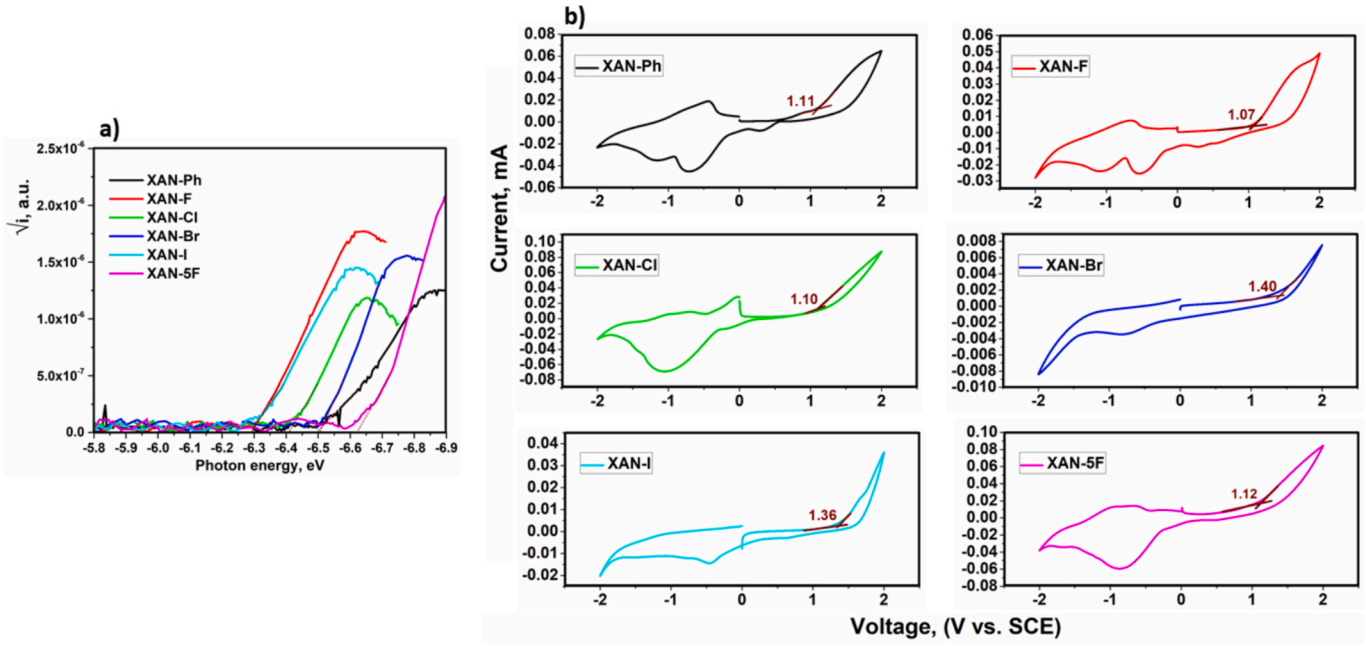

Fig. 5. a) Extracted IP plot of spin-coated XAN derivatives on the FTO and b) CV voltammograms of dissolved compounds in DCM.

the onset potentials of oxidation and reduction, respectively. The CV curves (Fig. 5b) show irreversible oxidation peaks for all derivatives, suggesting fast electron transfer processes. XAN-Br exhibited the lowest HOMO energy, reflecting its weakest electron donor capability. Furthermore, broad waves of reduction were observed during the negative potential trend, likely due to a combination of multiple reduction steps, structural reorganization upon electron uptake, and irreversible behavior in halogenated derivatives. Specifically, XAN-Ph exhibited a broad reduction peak due to delocalization effects in the reduced state. XAN-Br showed slow electron transfer kinetics likely due to weak orbital interactions or halide elimination effects and XAN-F and 5F exhibited strong solvation effects that contributed to broader reduction peaks. In addition, XAN-Cl and I showed irreversible reduction behavior possibly due to dissociation of Cl^- and I^- [40,41]. XAN-I also had the highest EA_{CV}, making it the most readily reduced. This behavior can be attributed to the weaker C—I bond, which facilitates partial dissociation or transition state stabilization during reduction, thereby increasing the EA_{CV} [42].

3.6. Photophysical properties

3.6.1. UV–vis study and optical spectroscopy

The UV–vis spectra of the XAN derivatives, in toluene and chloroform and spin-coated films, are shown in Fig. 6. Key photophysical parameters are summarized in Table 2. In toluene, the absorption spectra of all compounds are similar, with maximum π-π* absorption bands between 287 and 296 nm. In the solid state, absorption bands are generally blue-shifted due to the absence of solvent stabilization and the rigid molecular environment, which limits conformational relaxation and π–π stacking, thereby increasing the energy gap [43]. In films, XAN-Br shows the largest optical band gap (E_g^{Opt}=3.70 eV). This is attributed to weak orbital interactions, limited conjugation and molecular packing effects that reduce the efficiency of absorption of low energy photons [44]. All compounds exhibit blue photoluminescence in solution and in the solid state, except XAN-5F, which shifts toward green, with PL maxima ranging from 407 to 521 nm. Due to the multiple fluorine substitutions, XAN-5F both the HOMO and LUMO of XAN-5F are mainly distributed in the xanthene core, as shown in Fig. 1, which enhances the intramolecular charge transfer (ICT) and a red-shift in the PL emission from blue to green [45,46]. Photoluminescence (PL) spectra of the

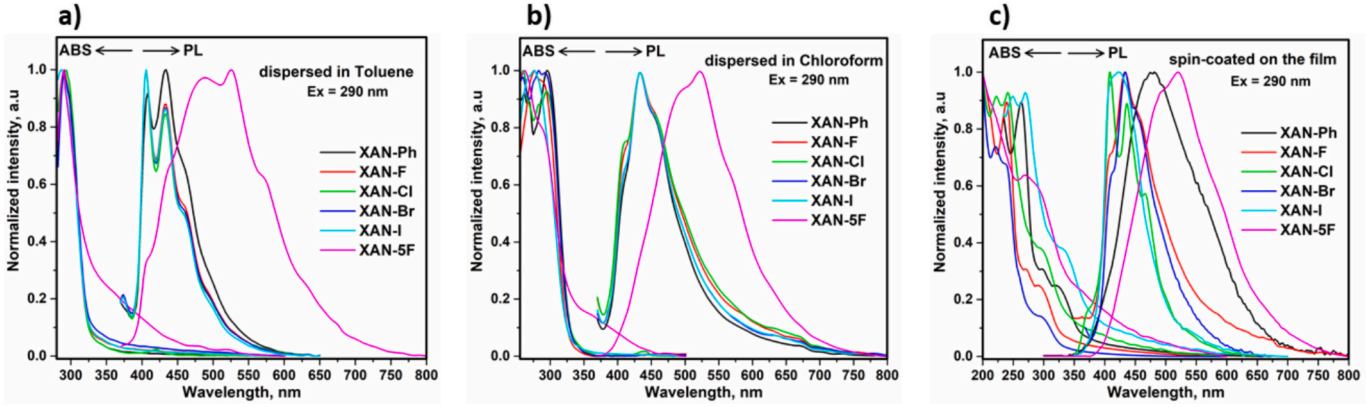

Fig. 6. Absorption and emission spectra of the dispersed compounds in a) toluene, b) chloroform and c) spin-coated on the films (99 wt% XAN derivative:1 wt % Zeonex).

Table 2
Photophysical parameters of XAN derivatives.

Compound	ABS^{max}, nm	PL^{max}, nm	τ, ns	χ^2	PLQY, %
	(Toluene/Chloroform/Film) in air				
XAN-Ph	291/ 296/262	(408, 432)/ (432)/(476)	(2.80)/(3.44)/ ($\tau_1 = 0.32$ and $\tau_2 = 7.20$)	1.16/ 1.07/ 1.12	2, >1, 6
XAN-F	290/ 277/239	(406, 432)/ (433)/(432)	(2.87)/(3.66)/ (433×10^4)	1.01/ 1.00/ 1.14	7, 1, 15
XAN-Cl	292/ 293/239	(405, 432)/ (433)/(407, 435)	(2.94)/(3.18)/ (450×10^4)	1.16/ 1.06/ 1.20	5, 1, 18
XAN-Br	290/ 283/223	(406, 433)/ (432)/(432)	(3.24)/(3.29)/ (404×10^4)	1.04/ 1.21/ 1.12	9, 3, 23
XAN-I	287/ 275/270	(406, 433)/ (432)/(423)	(2.81)/(3.32)/ (448×10^4)	1.16/ 1.16/ 1.11	12, 5, 25
XAN-5F	289/ 262/268	(486, 525)/ (522)/(521)	(2.97)/(3.03)/ (390×10^4)	1.18/ 1.11/ 1.18	5, >1, 16

compounds in toluene and chloroform show little solvatochromism, but mild vibronic structures are observed in toluene. This is due to the nonpolar nature of toluene, which preserves molecular vibrational modes and leads to resolved vibronic features, whereas the polar chloroform induces more electronic relaxation and less structured emission [47,48]. Photoluminescence quantum yields (PLQYs) were measured for all derivatives in solution and film, and the values are listed in Table 2. Higher PLQYs were observed in toluene than in chloroform, likely due to reduced CT interactions in nonpolar solvents [49]. Notably, the PLQYs increased significantly in spin-coated films. This enhancement is attributed to restricted intramolecular motions in the solid state, which reduces non-radiative decay pathways and facilitates aggregation-induced emission (AIE) [50].

3.6.2. PH and RTP mechanisms

PL decay curves for the XAN derivatives were recorded in toluene and chloroform solutions, as well as in spin-coated films containing 1 wt % Zeonex under ambient and vacuum conditions shown (Fig. 7). Zeonex was chosen as a binder to improve film quality because it is photophysically inert, enabling measurement of the emitters' intrinsic PL/RTP behavior with minimal influence from host polarity, packing, or specific interactions [51–53]. The corresponding constant lifetime (τ) is listed in Table 2. In solution, τ values were in the nanosecond (ns) range. Notably, compounds exhibited longer lifetimes in chloroform than in toluene, attributed to the stabilization of ICT states in the more polar chloroform, which favors non-radiative decay, reduces PLQY, and extends emission lifetimes, as described in Eqs. S1 and S2. In the solid state (Fig. 7c), XAN-Ph exhibited lifetimes of $\tau_1 = 0.32$ ns and $\tau_2 = 7.20$ ns (Table 2), indicative of prompt fluorescence [54]. Two lifetimes in solid films are caused by molecular interactions, aggregates, energy transfer or trap states. In solution, such effects are not present, so the decay is single exponential. As illustrated in the Jablonski diagram Fig. S3, charge transfer singlet (1CT) emission occurs throughout the entire decay process. Compared to delayed fluorescence and phosphorescence mechanisms, the reduced decay time in the ns region at room temperature is due to thermally induced surface defects, which may trigger deep trap emission or some non-radiative processes [55]. In stark contrast, thin films of the halogenated derivatives exhibited lifetimes ~10^6 times longer, falling into the millisecond (ms) range (Fig. 7d and Table 2), suggesting significant triplet-state involvement. Possible emissive mechanisms include phosphorescence (PH), room temperature phosphorescence (RTP), thermally activated delayed fluorescence

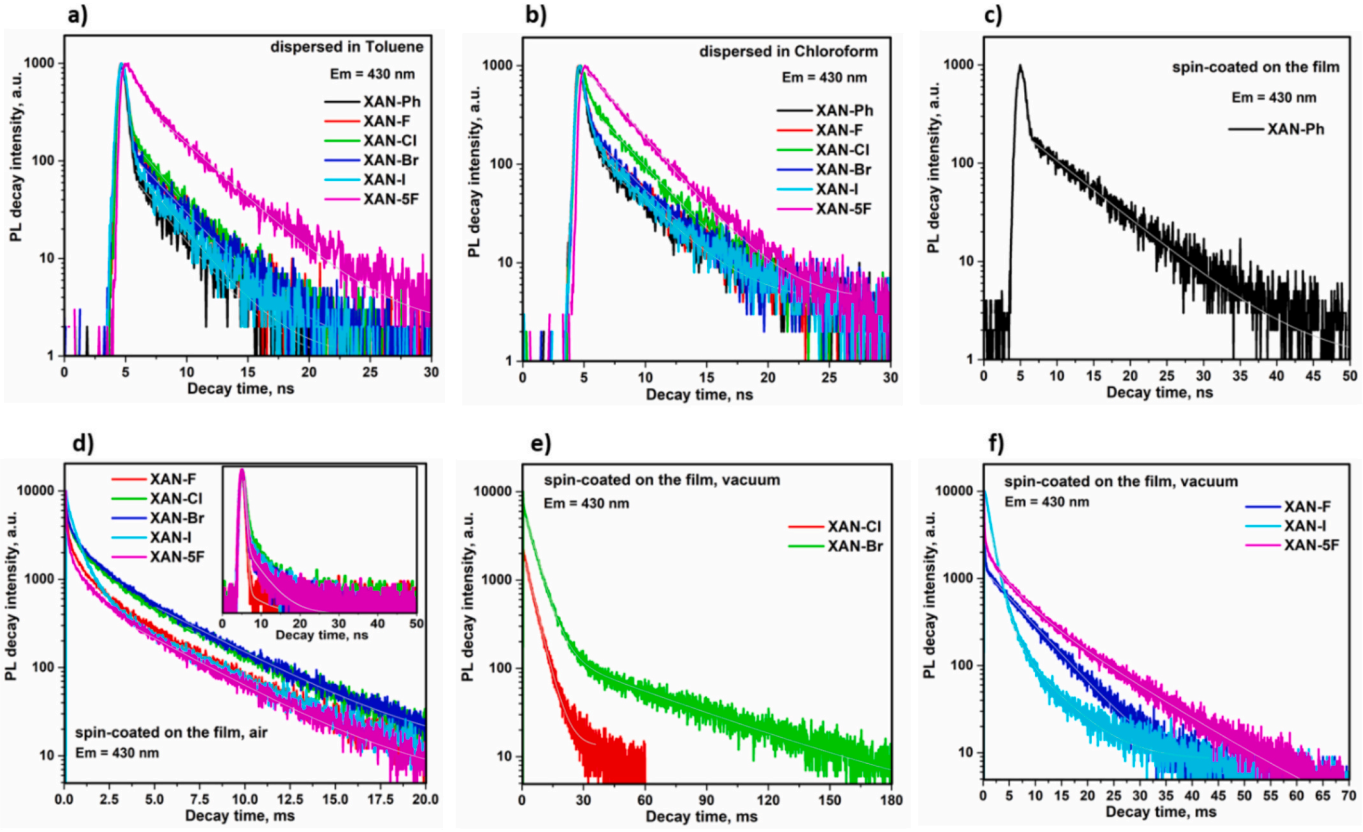

Fig. 7. Time-resolved PL decay curve of the XAN derivatives in a) toluene, b) chloroform, and spin-coated film (mixed 1 wt% Zeonex) in air c) XAN-Ph in air, d) XAN-Br, Cl, I, F, 5F in air e) XAN-Br, Cl and f) XAN-I, F, 5F.

(TADF) and triplet-triplet annihilation (TTA). To resolve these possibilities, PL and PH spectra at low-temperature (77 K) (Fig. 8) and the power dependence (Fig. S4) were measured. The energy difference between the first excited singlet state (S_1) and the first excited triplet state (T_1), ΔE_{ST}, was calculated from the onset spectra of PL and PH at 77 K. The large ΔE_{ST} excluded the TADF mechanism. In Fig. S4, the slopes of the log–log plot of integrated emission intensity vs. excitation power are smaller than 2, which rules out TTA [53,54]. XAN-Ph is drastically different from others, showing only FL due to its poor spin-orbit coupling. To distinguish between RTP and phosphorescence, PL spectra were recorded under both air and vacuum (5×10^{-7} bar) (Fig. S5). XAN-Ph, exhibiting only ns-range τ, and XAN-5F, with negligible change in $\frac{I_{PL}^{Vacuum}}{I_{PL}^{Air}}$ [56], are not considered RTP candidates. Conversely, XAN-Br and XAN-I showed dramatic increases in emission intensity under vacuum, with $\frac{I_{PL}^{Vacuum}}{I_{PL}^{Air}}$ values of 14.67 and 15.33, respectively. This enhancement indicates oxygen-sensitive triplet-state emission characteristic of RTP, as oxygen quenching is suppressed in vacuum. Heavy atom effects from Br and I promote strong SOC, as reported ξ_{ISC} values in Table S2 were in the range of 8.77×10^7 and 4.88×10^7 eVs^{-1} for Br and I, respectively. This increases the ISC, leading to a higher population of triplet states and thereby facilitating more efficient RTP [57]. Fig. S6 shows the normalized intensity of the PL spectra of the XAN-F, —Cl, —Br and —I films at room temperature, in an oxygen-free environment and the PH spectrum at 77 K. It is clear that the substitutions of XAN-Br and I stabilize the triplet states, the PL spectrum at RT and the PL spectrum in vacuum overlap for XAN-Ph, —F, —Cl and —5F. However, for XAN-Br and I, a second band appears in the PL spectra at RT under vacuum, which coincides with the area under the latter PH spectrum. Fig. S6 shows that for XAN-Br and XAN-I, the PL spectra at RT in air (black spectra) are dominated by prompt fluorescence from the excited singlet state (S_1), with little to no contribution from triplet states due to rapid non-radiative deactivation and oxygen quenching. Under vacuum conditions, the emission intensity increases significantly, and a red-shifted broad emission band appears, indicating the contribution of triplet states. This enhancement results from the removal of molecular oxygen, which otherwise acts as an efficient quencher of triplet states by collisional deactivation. It is noteworthy that ISC plays a crucial role in the efficient formation of the excited triplet state, a process that is significantly enhanced by SOC. XAN-Br and XAN-I exhibited high intersystem crossing quantum yield (Φ_{ISC}) values of 93.02 and 93.51 %, respectively, outperforming other derivatives. These findings confirm that XAN-Br and XAN-I undergo efficient RTP, while XAN-Ph is fluorescent and XAN-F, —Cl, and —5F exhibit primarily PH [12,58,59]. Other studies have also demonstrated RTP behavior in halogenated XAN derivatives [60–62]. Based on these observations, both XAN-Br and XAN-I are considered as potential ratiometric probes for oxygen sensing.

3.7. Oxygen sensing properties

To investigate the oxygen sensitivity of halogenated XAN derivatives, PL spectra (Ex = 290 nm and Em = 430 nm) of spin-coated films (200 μm thick) consisting of 1 wt% Zeonex were recorded at different oxygen concentrations. The corresponding PL spectra, CIE (Commission Internationale de l'Éclairage) coordinates, and visual imagea of the films in the chamber (evacuated and under O_2) are shown in Fig. 9. As oxygen concentration increased, PL intensity decreased significantly for XAN-F, —Br, —I, and —5F. For these haloganated XAN derivatives, upon excitation from the ground state (S_0) to a higher-energy singlet excited state (e.g., S_2), the molecules rapidly undergo IC to the first excited singlet state (S_1), followed by ISC to the triplet state T_1 (Fig. S3). This T_1 state is efficiently quenched by the surrounding oxygen molecule, leading to suppresssion of PH [63]. Notably, the phenyl and chlorophenyl substituents increase structural rigidity, which minimize the non-radiative pathways induced by oxygen by reducing

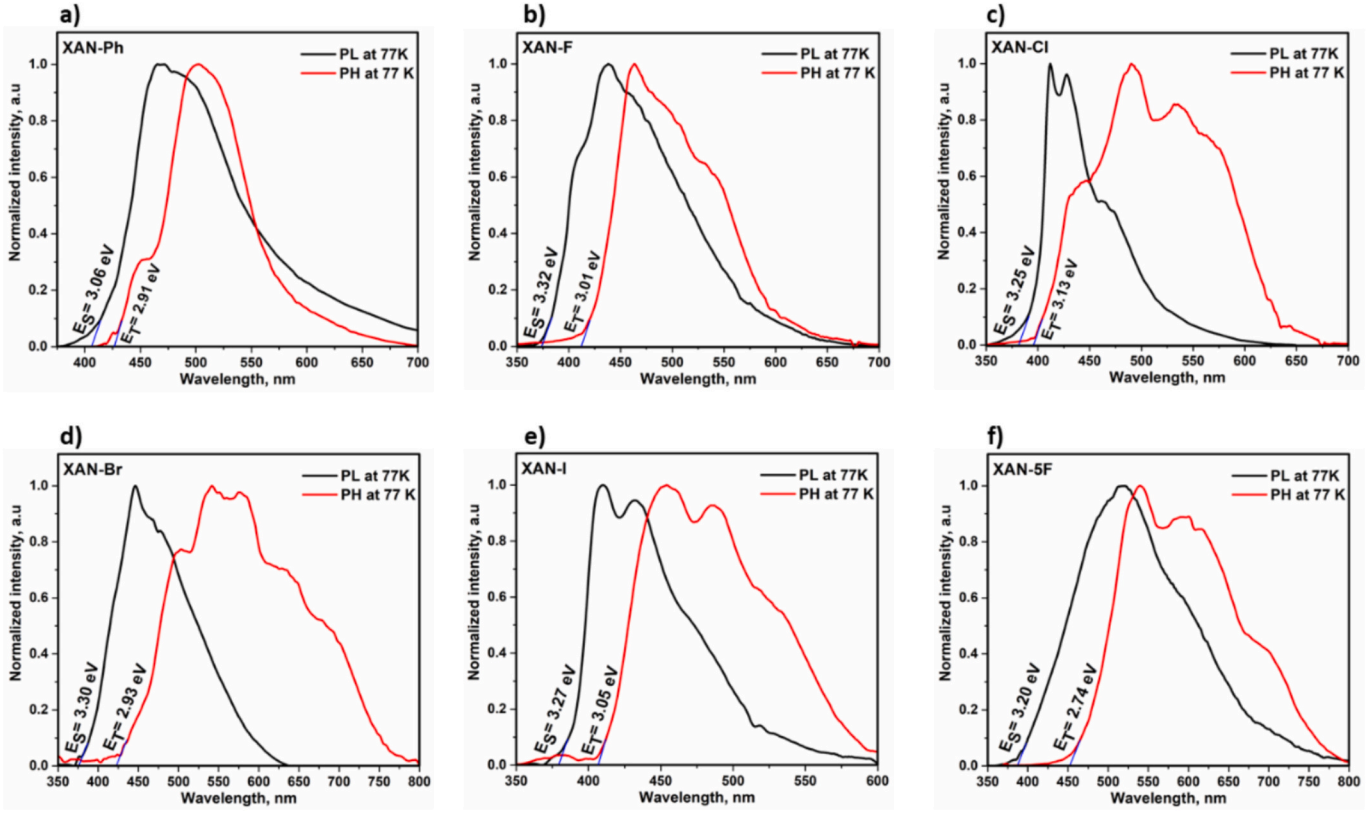

Fig. 8. PL and PH spectra of 99 wt% XAN derivative:1 wt% Zeonex films measured at 77 K.

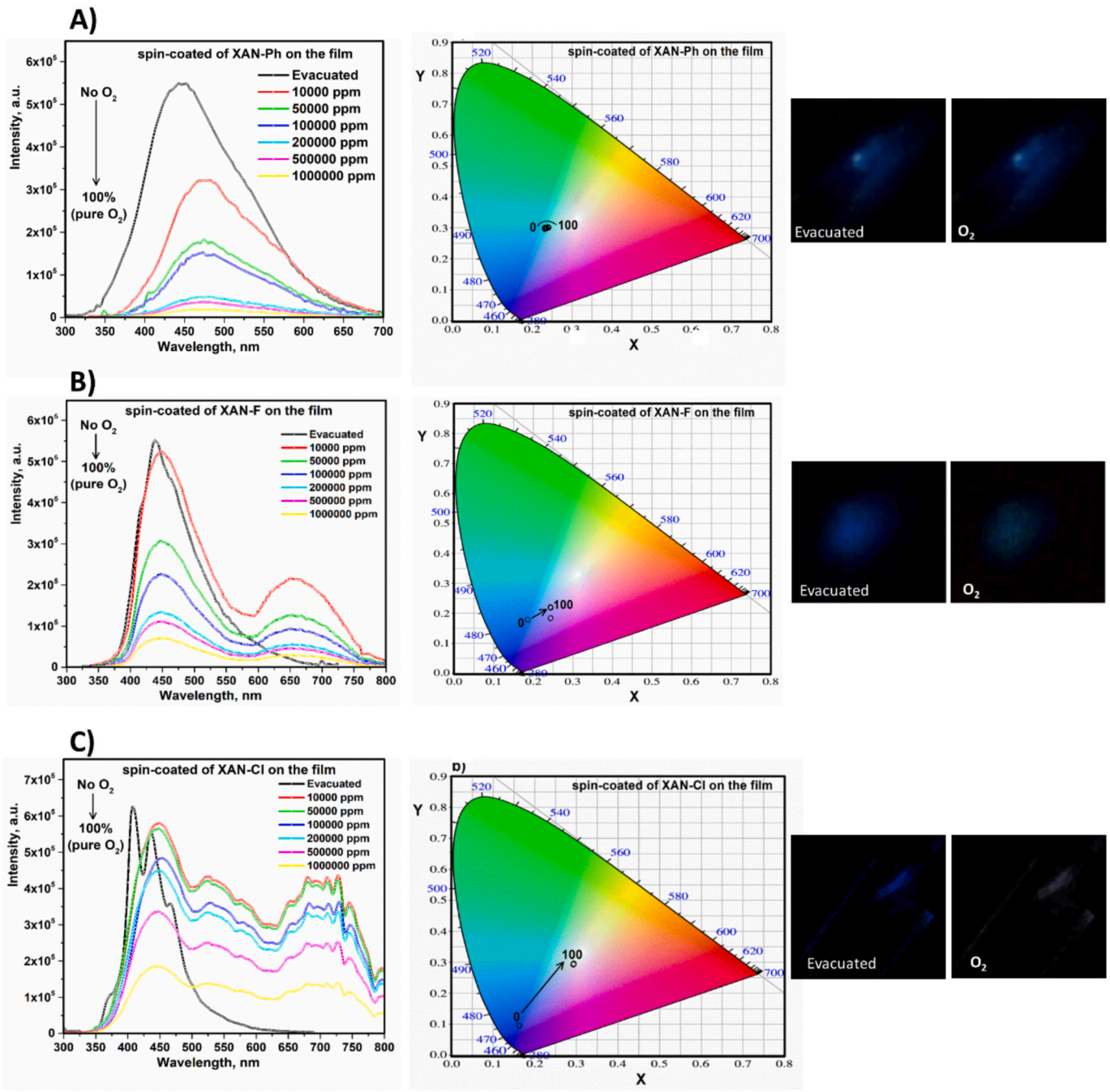

Fig. 9. PL spectra, CIE coordinates and photographs before and after the injection of oxygen gas of coated films (99 wt% XAN derivative, 1 wt% Zeonex) for A) XAN-Ph B) XAN-F C) XAN-Cl D) XAN-Br E) XAN-I, and F) XAN-5F. G) Stern-Volmer rate constants obtained from linear and nonlinear fits.

the ξ_{ISC} and moderting SOC (Table S2). To quantify fluorescence quenching, including the effects of oxygen, and assess the oxygen sensitivity of the XAN derivatives, Stern–Volmer analysis was performed using Eqs. (2) and (3):

$$\frac{\mathbf{A_0}}{\mathbf{A}} \sim \frac{\mathbf{I_0}}{\mathbf{I}} = \frac{\mathbf{I_0}}{\mathbf{I}} = 1 + K_{SV}[Q] \tag{2}$$

$$\frac{A_0}{A} \sim \frac{I_0}{I} = (1 + K_{SV_1}[Q])(1 + K_{SV_2}[Q]) \tag{3}$$

where I_0 is the PL intensity in an oxygen-free state, I is the PL intensity in an oxygen atmosphere, K_{SV} is the Stern-Volmer constant, and [Q] is the oxygen concentration (from 0 to 10^6 ppm in this study), and K_{SV_1} and K_{SV_2} correspond to dynamic and static Stern-Volmer quenching constants [64]. The PL integral area ratio ($\frac{A_0}{A}$) is considered proportional to the PL intensity ratio ($\frac{I_0}{I}$), when A_0 and A represent the PL spectrum area in an oxygen-free and in an oxygen atmosphere respectively. The nonlinearity observed in some Stern-Volmer plots is attributed to heterogeneities in the binding sites in the Zeonex matrix, leading to differences in the local oxygen quenching constants [65]. The observed variations in K_{SV} indicate differences in the interaction with molecular oxygen, which can be influenced by electronic effects, steric hindrance and the molecular environment [66]. Due to the linear fit of $\frac{I_0}{I}$ versus oxygen concentration plots for the XAN-Ph, F and Cl films (Fig. 9G), Eq. (2) was used to calculate their K_{SV} values (slopes) to be 2.96×10^{-5},

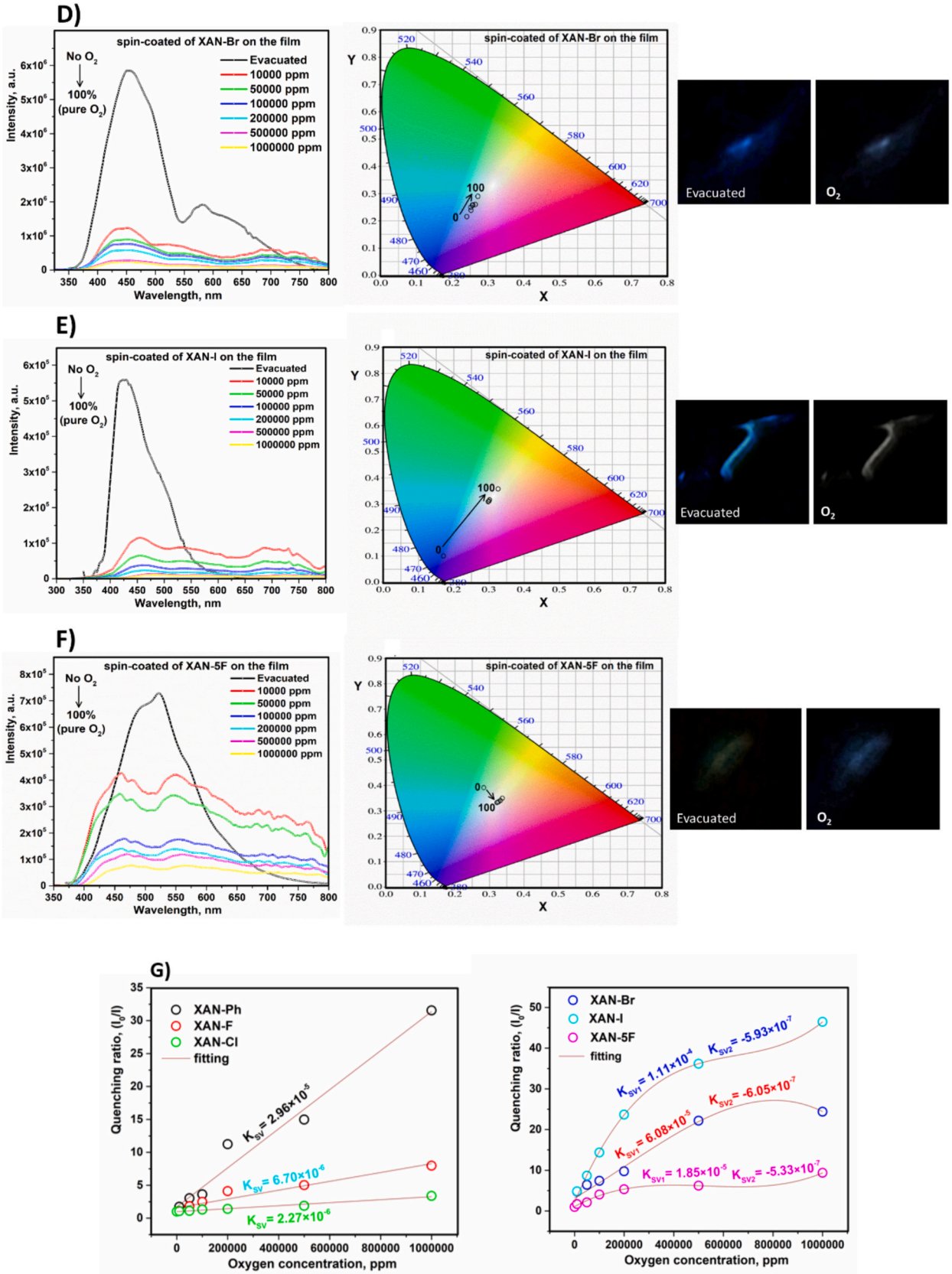

Fig. 9. (*continued*).

2.27 × 10^{-6}, and 6.70 × 10^{-6} ppm^{-1}, respectively. Although the K_{sv} values for XAN-F and XAN-Cl were relatively modest, both compounds exhibited strong sensitivity to oxygen, with significant quenching observed even at 10,000 ppm, suggesting strong interactions between molecular oxygen and the triplet excited state of these compounds. Molecular oxygen (O_2) is a well-known triplet quencher, which can

effectively quench long-lived triplet states, even when K_{sv} values moderate [67], as in the case of XAN-F and Cl. Interestingly, XAN-Ph showed greater oxygen sensitivity than halogenated derivatives such as XAN-F, XAN-Cl, and XAN-5F (Fig. 9B, C and F), suggesting that these halogen substitution on the phenyl ring does not significantly enhance K_{SV}. The high electronegativity of halogens (F > Cl > Br > I) results in the formation of strong, rigid, and hydrophobic C—F and C—Cl bonds, which reduce oxygen permeability and solubility. Although Cl is less electronegative than F, it similarly withdraws electron density, contributing to the same effect [68]. For XAN-Br, XAN-I, and XAN-5F, non-linear Stern–Volmer plots were observed (Fig. 9-G), and Eq. (3) was applied. The K_{SV_1} and K_{SV_2} values are 6.08×10^{-5} and -6.05×10^{-7} ppm^{-1} for XAN-Br, 1.11×10^{-4} and -5.93×10^{-7} ppm^{-1} for XAN-I and 1.85×10^{-5} and -5.33×10^{-7} ppm^{-1} for XAN-5F ppm^{-1}, respectively. Notably, both XAN-Br and XAN-I exhibit RTP, as confirmed by video evidence (see Supporting Information), and showed the highest K_{SV} values. Their longer RTP lifetimes are likely to promote prolonged interactions between triplet states and oxygen. Furthermore, the large atomic radius and polarizability of iodine can enhance non-covalent interactions, increasing oxygen accessibility [69]. XAN-Br also exhibits high quenching, though lower than XAN-I, which may be due to its slightly smaller atomic size and weaker electron donor capability. This study solved several challenges in oxygen sensing with the newly designed halogenated XAN derivatives, particularly XAN-Br and XAN-I, which exhibit RTP and excellent oxygen sensitivity. These materials are well suited for biological, environmental and industrial applications and also have potential for use in oxygen tunable delayed luminescence. However, in this study, the relatively simple synthesis route and significantly high sensitivity to oxygen, especially at low concentrations, are the main advantages. Notably, the characteristic shift in emission from blue/greenish to white with increasing oxygen concentration provides a visually observable, on-site detection method that requires no specialized equipment. The best-performing emitter, XAN-Br, shows an approximately linear quenching response to O_2 (Fig. 9G) with a large K_{SV}, making it well suited for low-cost sensing in applications in the range of 0–21 % O_2 (0–210,000 ppm), including tumor hypoxia imaging and blood-oxygen monitoring, environmental sensing, and food-safety monitoring [2,70–73]. However, sensitivity declines above ~21 % O_2, which is suboptimal for applications requiring higher ranges (e.g., high-O_2 food packaging and oxygen-enriched/oxy-fuel combustion) [74,75]. Tailoring the host/matrix to increase oxygen permeability may broaden the dynamic range [76–78].

4. Conclusions

Six XAN derivatives with different substituents on the phenyl group, XAN-Ph, XAN-F, XAN-Cl, XAN-Br, XAN-I and XAN-5F, were designed and synthesized to tune their optical oxygen sensing capabilities. The molecular design aimed to enhance spin–orbit coupling (SOC) and promoting intersystem crossing (ISC) to facilitate room-temperature phosphorescence (RTP). X-ray diffraction (XRD) confirmed high crystallinity in most derivatives, except XAN-F, which showed a mixed amorphous–crystalline nature with small crystallite sizes. Experimental results were consistent with density functional theory (DFT) calculations, with XAN-I exhibiting the highest HOMO energy level as determined by ionization potential (IP) measurements. The optical band gaps of the spin-coated films ranged from 3.11 to 3.70 eV, influenced by the nature of halogen substituents. Notably, the high excited triplet state (T_1) energies of XAN-Br and XAN-I ($\geq$ 2.93 eV) make them highly sensitive to oxygen. Their emission color changed from blue/greenish to white even at a low oxygen injection (e.g., 10000 ppm). Mechanistic analysis revealed that XAN-Ph followed a fluorescence (FL) mechanism, while XAN-F, XAN-Cl and XAN-5F showed phosphorescence (PH). In contrast, room temperature phosphorescence (RTP) was the dominant emission pathway for XAN-Br and XAN-I in an oxygen-free environment. RTP emission was further confirmed by excitation power–dependent emission slopes below 2, ruling out triplet–triplet annihilation. The PL-decay lifetime (τ) changed dramatically from nanoseconds for XAN-Ph to milliseconds for the halogenated derivatives, demonstrating that halogen substitution promotes triplet-state emission and significantly enhances oxygen sensitivity by facilitating ISC and $T_1 \rightarrow S_0$ transitions. The highest vacuum-to-air photoluminescence intensity ratio was 15.33 for XAN-I, indicating significant quenching by molecular oxygen. Furthermore, XAN-I exhibited the longest lifetime (τ = 4.48 ms) and the highest ISC quantum yield (Φ_{ISC}= 93.51 %), indicating a long-lived triplet state that enhances oxygen diffusion and quenching interactions and increases sensor sensitivity. Films of XAN-Br and XAN-I embedded in 1 wt% Zeonex showed superior oxygen sensitivity, with high Stern-Volmer constants (K_{SV_1}) of 6.08×10^{-5} ppm^{-1} for XAN-Br and 1.11×10^{-4} ppm^{-1} for XAN-I, respectively. Their superior oxygen response is attributed to long-lived RTP lifetimes, which facilitate efficient oxygen diffusion and triplet–triplet energy transfer. This study provides valuable insights into the design of purely organic RTP materials for oxygen sensing and demonstrates XAN-Br and XAN-I as promising metal-free, cost-effective, and highly sensitive candidates for optical oxygen sensors in biomedical, environmental, and wearable applications.

Supplementary data to this article can be found online at https://doi.org/10.1016/j.mseb.2025.118997.

CRediT authorship contribution statement

Mageshwari Anandan: Methodology, Investigation, Data curation. **Sohrab Nasiri:** Writing – original draft, Methodology, Investigation, Formal analysis, Conceptualization. **Praveen B. Managutti:** Software, Data curation. **Sharmarke Mohamed:** Software, Investigation, Data curation. **Jean Michel Nunzi:** Validation, Investigation. **Venkatramaiah Nutalapati:** Writing – review & editing, Validation, Supervision. **Yuning Li:** Writing – review & editing, Validation, Supervision, Resources, Investigation, Funding acquisition.

Declaration of competing interest

The authors declare that they have no known competing financial interests or personal relationships that could have appeared to influence the work reported in this paper.

No Financial interests or personal relationships.

Acknowledgments

This work was supported by the Natural Sciences and Engineering Research Council of Canada (RGPIN-2022-03835).

Data availability

Data will be made available on request.

References

[1] R. Ramamoorthy, P.K. Dutta, S.A. Akbar, Oxygen sensors: materials, methods, designs and applications, J. Mater. Sci. 38 (2003) 4271–4282, https://doi.org/10.1023/A:1026370729205.

[2] O. Trédan, C.M. Galmarini, K. Patel, I.F. Tannock, Drug resistance and the solid tumor microenvironment, JNCI J. Natl. Cancer Inst. 99 (2007) 1441–1454, https://doi.org/10.1093/JNCI/DJM135.

[3] R.I. Dmitriev, D.B. Papkovsky, Optical probes and techniques for O2 measurement in live cells and tissue, Cell. Mol. Life Sci. 6912 (69) (2012), https://doi.org/10.1007/S00018-011-0914-0, 2025–2039.

[4] X.D. Wang, O.S. Wolfbeis, Optical methods for sensing and imaging oxygen: materials, spectroscopies and applications, Chem. Soc. Rev. 43 (2014) 3666–3761, https://doi.org/10.1039/C4CS00039K.

[5] I. Sánchez-Barragán, J.M. Costa-Fernández, A. Sanz-Medel, M. Valledor, J. C. Campo, Room-temperature phosphorescence (RTP) for optical sensing, TrAC, Trends Anal. Chem. 25 (2006) 958–967, https://doi.org/10.1016/J.TRAC.2006.07.009.

[6] X. Jia, C. Shao, X. Bai, Q. Zhou, B. Wu, L. Wang, B. Yue, H. Zhu, L. Zhu, Photoexcitation-controlled self-recoverable molecular aggregation for flicker phosphorescence, Proc. Natl. Acad. Sci. USA 116 (2019) 4816–4821, https://doi.org/10.1073/PNAS.1821991116.

[7] W. Zhao, Z. He, B.Z. Tang, Room-temperature phosphorescence from organic aggregates, Nat. Rev. Mater. 512 (5) (2020) 869–885, https://doi.org/10.1038/s41578-020-0223-z.

[8] Y.C. Liang, Y. Shang, K.K. Liu, Z. Liu, W.J. Wu, Q. Liu, Q. Zhao, X.Y. Wu, L. Dong, C.X. Shan, Water-induced ultralong room temperature phosphorescence by constructing hydrogen-bonded networks, Nano Res 13 (2020) 875–881, https://doi.org/10.1007/S12274-020-2710-3.

[9] O. Bolton, K. Lee, H.J. Kim, K.Y. Lin, J. Kim, Activating efficient phosphorescence from purely organic materials by crystal design, Nat. Chem. 3 (2011) 205–210, https://doi.org/10.1038/NCHEM.984.

[10] M. Gmelch, H. Thomas, F. Fries, S. Reineke, Programmable transparent organic luminescent tags, Sci. Adv. 5 (2019), https://doi.org/10.1126/SCIADV.AAU7310.

[11] A. Cheng, H. Su, X. Gu, W. Zhang, B. Zhang, M. Zhou, J. Jiang, X. Zhang, G. Zhang, Disorder-enhanced charge-transfer-mediated room-temperature phosphorescence in polymer media, Angew. Chem. Int. Ed. 62 (2023) e202312627, https://doi.org/10.1002/ANIE.202312627.

[12] Y. Gong, J. Yang, M. Fang, Z. Li, Room-temperature phosphorescence from metal-free polymer-based materials, Cell Reports Phys. Sci. 3 (2022), https://doi.org/10.1016/j.xcrp.2021.100663.

[13] J. Peng, S. Sokolov, D. Hernangómez-Pérez, F. Evers, L. Gross, J.M. Lupton, J. Repp, Atomically resolved single-molecule triplet quenching, Science 80 (373) (2021) 452–456, https://doi.org/10.1126/SCIENCE.ABH1155.

[14] H. Zheng, Z. Zhang, S. Cai, Z. An, W. Huang, Enhancing purely organic room temperature phosphorescence via supramolecular self-assembly, Adv. Mater. 36 (2024) 2311922, https://doi.org/10.1002/ADMA.202311922.

[15] X.D. Wang, O.S. Wolfbeis, Optical methods for sensing and imaging oxygen: materials, spectroscopies and applications, Chem. Soc. Rev. 43 (2014) 3666–3761, https://doi.org/10.1039/C4CS00039K.

[16] L. Zang, H. Zhao, Lutetium-containing sinoporphyrin sodium: a water-soluble photosensitizer with balanced fluorescence and phosphorescence for ratiometric oxygen sensing, RSC Adv. 10 (2020) 32938–32945, https://doi.org/10.1039/D0RA05400C.

[17] Y. Zhou, W. Qin, C. Du, H. Gao, F. Zhu, G. Liang, Long-lived room-temperature phosphorescence for visual and quantitative detection of oxygen, Angew. Chem. Int. Ed. 58 (2019) 12102–12106, https://doi.org/10.1002/ANIE.201906312.

[18] Z. Wu, K. Bergmann, Z.M. Hudson, Dopants induce persistent room temperature phosphorescence in triarylamine Boronate esters, Angew. Chem. Int. Ed. 63 (2024) e202319089, https://doi.org/10.1002/ANIE.202319089.

[19] E. Hamzehpoor, C. Ruchlin, Y. Tao, C.H. Liu, H.M. Titi, D.F. Perepichka, Efficient room-temperature phosphorescence of covalent organic frameworks through covalent halogen doping, Nat. Chem. 151 (15) (2022) 83–90, https://doi.org/10.1038/s41557-022-01070-4.

[20] H. Kato, K. Komagoe, Y. Nakanishi, T. Inoue, T. Katsu, Xanthene dyes induce membrane permeabilization of Bacteria and erythrocytes by photoinactivation, Photochem. Photobiol. 88 (2012) 423–431, https://doi.org/10.1111/J.1751-1097.2012.01080.X.

[21] L. Sobotta, P. Skupin-Mrugalska, J. Piskorz, J. Mielcarek, Non-porphyrinoid photosensitizers mediated photodynamic inactivation against bacteria, Dyes Pigments 163 (2019) 337–355, https://doi.org/10.1016/J.DYEPIG.2018.12.014.

[22] F. Morikawa, M. Fukuda, M. Naganuma, Y. Nakayama, Phototoxic reaction to xanthene dyes induced by visible light, J. Dermatol. 3 (1976) 59–67, https://doi.org/10.1111/J.1346-8138.1976.TB00973.X.

[23] M.J. Frisch, J.A. Pople, J.S. Binkley, Self-consistent molecular orbital methods 25. Supplementary functions for gaussian basis sets, J. Chem. Phys. 80 (1984) 3265–3269, https://doi.org/10.1063/1.447079.

[24] L. Pilia, Y. Shuku, S. Dalgleish, K. Awaga, N. Robertson, Structural and electronic effects due to fluorine atoms on Dibenzotetraaza-annulenes complexes, ACS Omega 3 (2018) 10074–10083, https://doi.org/10.1021/ACSOMEGA.8B01442.

[25] P.W. Atkins (Ed.), Quanta: A Handbook of Concepts, Oxford University Press, 1994. ISBN-10. 9780198555735.

[26] S. Brend'amour, J. Gilmer, M. Bolte, H.W. Lerner, M. Wagner, C-halogenated 9,10-Diboraanthracenes: how the halogen load and distribution influences key optoelectronic properties, Chem. – A Eur. J. 24 (2018) 16910–16918, https://doi.org/10.1002/CHEM.201804288.

[27] Y. Mao, M. Head-Gordon, Y. Shao, Unraveling substituent effects on frontier orbitals of conjugated molecules using an absolutely localized molecular orbital based analysis, Chem. Sci. 9 (2018) 8598–8607, https://doi.org/10.1039/C8SC02990C.

[28] G.P. Kissling, B. Ruhstaller, K.P. Pernstich, Measuring frontier orbital energy levels of OLED materials using cyclic voltammetry in solution, Org. Electron. 122 (2023) 106888, https://doi.org/10.1016/J.ORGEL.2023.106888.

[29] S. Nasiri, A. Dashti, M. Hosseinnezhad, M. Rabiei, A. Palevicius, A. Doustmohammadi, G. Janusas, Mechanochromic and thermally activated delayed fluorescence dyes obtained from D–A–D′ type, consisted of xanthen and carbazole derivatives as an emitter layer in organic light emitting diodes, Chem. Eng. J. 430 (2022) 131877, https://doi.org/10.1016/J.CEJ.2021.131877.

[30] B. Banerjee, M. Kaur, V. Sharma, V.K. Gupta, J. Kaur, A. Sharma, A. Priya, A. Singh, Camphor sulfonic acid catalyzed one-pot pseudo three-component synthesis of a series of 1,8-dioxo-octahydroxanthenes and comparative crystal structures investigations and Hirshfeld surface analysis of five such derivatives, Res. Chem. Intermed. 49 (2023) 4639–4670, https://doi.org/10.1007/S11164-023-05064-W.

[31] N.C. Miller, E. Cho, M.J.N. Junk, R. Gysel, C. Risko, D. Kim, S. Sweetnam, C. E. Miller, L.J. Richter, R.J. Kline, M. Heeney, I. McCulloch, A. Amassian, D. Acevedo-Feliz, C. Knox, M.R. Hansen, D. Dudenko, B.F. Chmelka, M.F. Toney, J. L. Brédas, M.D. McGehee, Use of X-ray diffraction, molecular simulations, and spectroscopy to determine the molecular packing in a polymer-fullerene bimolecular crystal, Adv. Mater. 24 (2012) 6071–6079, https://doi.org/10.1002/ADMA.201202293.

[32] M. Rabiei, A. Palevicius, A. Monshi, S. Nasiri, A. Vilkauskas, G. Janusas, Comparing methods for calculating nano crystal size of natural hydroxyapatite using X-ray diffraction, Nanomater 10 (2020) 1627, https://doi.org/10.3390/NANO10091627.

[33] J. Calvo-Castro, G. Morris, A.R. Kennedy, C.J. McHugh, Effects of fluorine substitution on the intermolecular interactions, energetics, and packing behavior of N-benzyl substituted Diketopyrrolopyrroles, Cryst. Growth Des. 16 (2016) 2371–2384, https://doi.org/10.1021/ACS.CGD.6B00157.

[34] A. Ebadi, A. Karimi, A. Bahmani, Z. Najafi, G. Chehardoli, Novel Xanthene-1,8-dione derivatives containing the benzylic ether tail as potent cytotoxic agents: design, synthesis, in vitro, and in silico studies, J. Chemother. 2024 (2024) 6612503, https://doi.org/10.1155/2024/6612503.

[35] A. Elmekawy, Q. Quach, T.M. Abdel-Fattah, Synthesis and characterization of silver-modified Nanoporous silica materials for enhanced iodine removal, Nanomaterials 14 (2024) 1143, https://doi.org/10.3390/NANO14131143.

[36] P.C. Blainey, P.J. Reid, FTIR studies of intermolecular hydrogen bonding in halogenated ethanols, Spectrochim. Acta Part A Mol. Biomol. Spectrosc. 57 (2001) 2763–2774, https://doi.org/10.1016/S1386-1425(01)00507-8.

[37] A. Saeed, G. Shabir, S.A. Shehzadi, Synthesis and characterization of new xanthene derivatives, and their electrochemical study, J. Chin. Chem. Soc. 63 (2016) 181–188, https://doi.org/10.1002/JCCS.201500345.

[38] M. Sima Abdollahi, E. Nemati-Kande, A. Poursattar Marjani, Experimental and DFT studies on the FT-IR, NMR and UV/Vis spectra of a xanthene derivative: the case of 9-benzoyl-3,4,5,6,7,9-hexahydro-1h-xanthene-1,8(2h)-dione, ChemistrySelect 5 (2020) 3971–3980, https://doi.org/10.1002/SLCT.201904165.

[39] Y.A. Kurskii, N.M. Khamaletdinova, A.N. Egorochkin, Polarizability constant of iodine as substituent in correlation analysis, Russ. J. Gen. Chem. 87 (2017) 1651–1655, https://doi.org/10.1134/S1070363217080011.

[40] N. Elgrishi, K.J. Rountree, B.D. McCarthy, E.S. Rountree, T.T. Eisenhart, J. L. Dempsey, A practical beginner's guide to cyclic voltammetry, J. Chem. Educ. 95 (2018) 197–206, https://doi.org/10.1021/ACS.JCHEMED.7B00361.

[41] J.A. Beeler, R.P. Walkingshaw, S.A.S. Hamud, H.S. White, Reduction by oxidation: selective Hydrodehalogenation of aryl halides by mediated oxalate oxidation, J. Am. Chem. Soc. 147 (2025) 12206–12217, https://doi.org/10.1021/jacs.5c01366.

[42] T. Sengupta, M.S. Khan, S. Pal, Mechanistic investigation of the carbon-iodine bond activation on the niobium-carbon cluster, ACS Omega 2 (2017) 5335–5347, https://doi.org/10.1021/ACSOMEGA.7B00894.

[43] Š. Budzák, A.D. Laurent, C. Laurence, M. Medved', D. Jacquemin, Solvatochromic shifts in UV–vis absorption spectra: the challenging case of 4-nitropyridine N-oxide, J. Chem. Theory Comput. 12 (2016) 1919–1929, https://doi.org/10.1021/ACS.JCTC.6B00149.

[44] C.Z. Zhang, T. Li, Y. Yuan, C.Y. Gu, M.X. Niu, H. Cao, Effect of bromine substituent on optical properties of aryl compounds, J. Phys. Org. Chem. 30 (2017) e3620, https://doi.org/10.1002/POC.3620.

[45] M. Morita, S. Yamada, T. Konno, Systematic studies on the effect of fluorine atoms in fluorinated Tolanes on their photophysical properties, Molecules 26 (2021) 2274, https://doi.org/10.3390/molecules26082274.

[46] H. Li, H. Li, J. Gu, F. He, H. Peng, Y. Tao, D. Tian, Q. Yang, P. Li, C. Zheng, W. Huang, R. Chen, Fluorine-induced aggregate-interlocking for color-tunable organic afterglow with a simultaneously improved efficiency and lifetime, Chem. Sci. 12 (2021) 3580–3586, https://doi.org/10.1039/D0SC06025A.

[47] D. Patra, C. Barakat, Synchronous fluorescence spectroscopic study of solvatochromic curcumin dye, Spectrochim, Acta Part A Mol. Biomol. Spectrosc. 79 (2011) 1034–1041, https://doi.org/10.1016/J.SAA.2011.04.016.

[48] H. Tanaka, K. Shizu, H. Nakanotani, C. Adachi, Dual intramolecular charge-transfer fluorescence derived from a phenothiazine-triphenyltriazine derivative, J. Phys. Chem. C 118 (2014) 15985–15994, https://doi.org/10.1021/JP501017F.

[49] S. Ellinger, K.R. Graham, P. Shi, R.T. Farley, T.T. Steckler, R.N. Brookins, P. Taranekar, J. Mei, L.A. Padilha, T.R. Ensley, H. Hu, S. Webster, D.J. Hagan, E. W. Van Stryland, K.S. Schanze, J.R. Reynolds, Donor-acceptor-donor-based π-conjugated oligomers for nonlinear optics and near-IR emission, Chem. Mater. 23 (2011) 3805–3817, https://doi.org/10.1021/CM201424A.

[50] T. Usuki, M. Shimada, Y. Yamanoi, T. Ohto, H. Tada, H. Kasai, E. Nishibori, H. Nishihara, Aggregation-induced emission enhancement from Disilane-bridged donor-acceptor-donor Luminogens based on the triarylamine functionality, ACS Appl. Mater. Interfaces 10 (2018) 12164–12172, https://doi.org/10.1021/acsami.7b14802.

[51] K. Stavrou, L.G. Franca, A.P. Monkman, Photophysics of TADF guest-host systems: introducing the idea of hosting potential, ACS Appl. Electron. Mater. 2 (2020) 2868–2881, https://doi.org/10.1021/ACSAELM.0C00514.

[52] P.L. Santos, J.S. Ward, P. Data, A.S. Batsanov, M.R. Bryce, F.B. Dias, A. P. Monkman, Engineering the singlet–triplet energy splitting in a TADF molecule, J. Mater. Chem. C 4 (2016) 3815–3824, https://doi.org/10.1039/C5TC03849A.

[53] P. Zimmermann Crocomo, T. Kaihara, S. Kawaguchi, P. Stachelek, S. Minakata, P. de Silva, P. Data, Y. Takeda, The impact of c2 insertion into a carbazole donor on the physicochemical properties of dibenzo[a,j]phenazine-cored donor–acceptor–donor triads, Chem. – A Eur. J. 27 (2021) 13390–13398, https://doi.org/10.1002/CHEM.202101654.

[54] S. Nasiri, M. Rabiei, H. Shaki, M. Hosseinnezhad, K. Kalyani, A. Palevicius, A. Vilkauskas, G. Janusas, V. Nutalapati, S. Kment, J. Michel Nunzi, What is TADF (thermally activated delayed fluorescence) compared to the mechanisms of FL (fluorescence), PH (phosphorescence), and TTA (triplet–triplet annihilation) based on a novel naphthalimide sulfonylphenyl derivative as a host? J. Photochem. Photobiol. A Chem. 447 (2024) 115289 https://doi.org/10.1016/J.JPHOTOCHEM.2023.115289.

[55] S.A. Crooker, T. Barrick, J.A. Hollingsworth, V.I. Klimov, Multiple temperature regimes of radiative decay in CdSe nanocrystal quantum dots: intrinsic limits to the dark-exciton lifetime, Appl. Phys. Lett. 82 (2003) 2793, https://doi.org/10.1063/1.1570923.

[56] X. Zhang, B. Zhang, J. Luo, S. Guo, C. Wei, Y. Gong, Room temperature phosphorescence emission from multi-states, Front. Chem. 9 (2022) 810458, https://doi.org/10.3389/FCHEM.2021.810458.

[57] J. Graton, S. Rahali, J.Y. Le Questel, G. Montavon, J. Pilmé, N. Galland, Spin–orbit coupling as a probe to decipher halogen bonding, Phys. Chem. Chem. Phys. 20 (2018) 29616–29624, https://doi.org/10.1039/C8CP05690K.

[58] X. Ma, J. Wang, H. Tian, Assembling-induced emission: An efficient approach for amorphous metal-free organic emitting materials with room-temperature phosphorescence, Acc. Chem. Res. 52 (2019) 738–748, https://doi.org/10.1021/ACS.ACCOUNTS.8B00620.

[59] J.M. Lee, S. Kang, T.G. Hwang, H.M. Kim, W.S. Lee, D. Kim, J.P. Kim, A study on photophysical and photodynamic properties of donor–acceptor BODIPY complexes: correlation between singlet oxygen quantum yield and singlet-triplet energy gap, Dyes Pigments 187 (2021) 109051, https://doi.org/10.1016/J.DYEPIG.2020.109051.

[60] Q. Liao, Q. Gao, J. Wang, Y. Gong, Q. Peng, Y. Tian, Y. Fan, H. Guo, D. Ding, Q. Li, Z. Li, 9,9-Dimethylxanthene derivatives with room-temperature phosphorescence: substituent effects and emissive properties, Angew. Chem. Int. Ed. 59 (2020) 9946–9951, https://doi.org/10.1002/ANIE.201916057.

[61] Y. Wang, H. Liu, Y. Song, L. Lin, Y. Xu, C.K. Wang, J. Fan, How structure and hydrostatic pressure impact excited-state properties of organic room-temperature phosphorescence molecules: a theoretical perspective, J. Phys. Chem. A 129 (2025) 502, https://doi.org/10.1021/ACS.JPCA.4C06952.

[62] A.E.R. Watson, S.Y. Tao, A. Siemiarczuk, P.D. Boyle, P.J. Ragogna, J.B. Gilroy, Organic room temperature Phosphorescence from BN-substituted xanthene derivatives, Angew. Chem. Int. Ed. 64 (2025) e202414534, https://doi.org/10.1002/ANIE.202414534.

[63] H. Zhang, T. Liu, X. Zhang, H. Zhao, Y. Zheng, F. Qin, Z. Zhang, T. Sheng, Y. Tian, An effective oxygen content detection in phosphorescence of PtOEP-C6/poly (St-co-TFEMA), Spectrochim, Acta Part A Mol. Biomol. Spectrosc. 257 (2021) 119786, https://doi.org/10.1016/J.SAA.2021.119786.

[64] Z. Yang, S. Zhao, X. Zhang, M. Liu, H. Liu, B. Yang, Efficient room-temperature phosphorescence from discrete molecules based on thianthrene derivatives for oxygen sensing and detection, Front. Chem. 9 (2022) 810304, https://doi.org/10.3389/FCHEM.2021.810304.

[65] W.W.S. Lee, K.Y. Wong, X.M. Li, Y.B. Leung, C.S. Chan, K.S. Chan, Halogenated platinum porphyrins as sensing materials for luminescence-based oxygen sensors, J. Mater. Chem. 3 (1993) 1031–1035, https://doi.org/10.1039/JM9930301031.

[66] Y. Feng, J. Cheng, L. Zhou, X. Zhou, H. Xiang, Ratiometric optical oxygen sensing: a review in respect of material design, Analyst 137 (2012) 4885–4901, https://doi.org/10.1039/C2AN35907C.

[67] S. Pullen, Oxygen tolerance in triplet-excited-state-based photocatalysis through compartmentalization, Chem Catal. 3 (2023) 100861, https://doi.org/10.1016/j.checat.2023.100861.

[68] G. Cavallo, P. Metrangolo, R. Milani, T. Pilati, A. Priimagi, G. Resnati, G. Terraneo, The halogen bond, Chem. Rev. 116 (2016) 2478–2601, https://doi.org/10.1021/ACS.CHEMREV.5B00484.

[69] G. Zhang, G.M. Palmer, M.W. Dewhirst, C.L. Fraser, A dual-emissive-materials design concept enables tumour hypoxia imaging, Nat. Mater. 89 (8) (2009) 747–751, https://doi.org/10.1038/nmat2509.

[70] R.I. Dmitriev, D.B. Papkovsky, Optical probes and techniques for O2 measurement in live cells and tissue, Cell. Mol. Life Sci. 6912 (69) (2012), https://doi.org/10.1007/S00018-011-0914-0, 2025–2039.

[71] C.M. Penso, J.L. Rocha, M.S. Martins, P.J. Sousa, V.C. Pinto, G. Minas, M.M. Silva, L.M. Goncalves, PtOEP–PDMS-based optical oxygen sensor, Sensors 21 (2021) 5645, https://doi.org/10.3390/S21165645.

[72] Y. Feng, J. Cheng, L. Zhou, X. Zhou, H. Xiang, Ratiometric optical oxygen sensing: a review in respect of material design, Analyst 137 (2012) 4885–4901, https://doi.org/10.1039/C2AN35907C.

[73] D.B. Papkovsky, R.I. Dmitriev, Biological detection by optical oxygen sensing, Chem. Soc. Rev. 42 (2013) 8700–8732, https://doi.org/10.1039/C3CS60131E.

[74] Y. Peng, K. Adhiputra, A. Padayachee, H. Channon, M. Ha, R.D. Warner, High oxygen modified atmosphere packaging negatively influences consumer acceptability traits of pork, Foods 8 (2019) 567, https://doi.org/10.3390/FOODS8110567.

[75] P. Skryja, I. Hudak, J. Bojanovsky, Z. Jegla, L. Korček, Effects of oxygen-enhanced combustion methods on combustion characteristics of non-premixed swirling flames, Energies 15 (2022) 2292, https://doi.org/10.3390/EN15062292.

[76] K. Koren, L. Hutter, B. Enko, A. Pein, S.M. Borisov, I. Klimant, Tuning the dynamic range and sensitivity of optical oxygen-sensors by employing differently substituted polystyrene-derivatives, Sensors Actuators B Chem. 176 (2013) 344–350, https://doi.org/10.1016/J.SNB.2012.09.057.

[77] K. Zhang, S. Lu, Z. Qu, X. Feng, Tuning the sensitivity and dynamic range of optical oxygen sensing films by blending various polymer matrices, Biosensors 12 (2022) 5, https://doi.org/10.3390/BIOS12010005/S1.

[78] E. Armagan, K. Wei, G. Fortunato, E. Amstad, R.M. Rossi, Reversible and broad-range oxygen sensing based on purely organic long-lived photoemitters, ACS Appl. Polym. Mater. 3 (2021) 2480–2488, https://doi.org/10.1021/ACSAPM.1C00064.